

Kinetic Sunyaev Zel’dovich velocity reconstruction from Planck and unWISE

Richard Bloch* and Matthew C. Johnson†

*Department of Physics and Astronomy, York University, Toronto, Ontario and
Perimeter Institute for Theoretical Physics, 31 Caroline St N, Waterloo, ON N2L 2Y5, Canada*

(Dated: May 3, 2024)

The kinetic Sunyaev Zel’dovich (kSZ) effect is a blackbody cosmic microwave background (CMB) temperature anisotropy induced by Thomson scattering off free electrons in bulk motion with respect to the CMB rest frame. The statistically anisotropic cross-correlation between the CMB and galaxy surveys encodes the radial bulk velocity (more generally, the remote dipole field), which can be efficiently reconstructed using a quadratic estimator. Here, we develop and implement a quadratic estimator for the remote dipole field to data from the Planck satellite and the unWISE galaxy redshift catalog. With this data combination, we forecast a $\sim 1\text{-}\sigma$ detection within ΛCDM assuming a simple model for the distribution of free electrons. Using reconstructions based on individual frequency temperature maps, we characterize the impact of foregrounds, concluding that they can be effectively mitigated by masking and removing the estimator monopole. We demonstrate that reconstructions based on component-separated CMB maps have no detectable biases from foregrounds or systematics at the level of the expected statistical error. We use these reconstructions to constrain the multiplicative optical depth bias to $b_v < 1.40$ at 68% confidence. Our fiducial signal model with $b_v = 1$ is consistent with this measurement. Our results support an optimistic future for kSZ velocity reconstruction with near-term datasets.

Keywords: CMB, Planck, LSS, kinetic Sunyaev-Zeldovich effect

I. INTRODUCTION

Over the past three decades ever-more sensitive measurements of the Cosmic Microwave Background (CMB) have allowed us to gain unparalleled insight into the physics of the early universe. The Planck satellite [1] has measured temperature anisotropies on the largest angular scales, the ‘primary’ CMB, to their cosmic variance limit. These measurements firmly established the standard cosmological model - ΛCDM . The new frontier in CMB science lies in the high-resolution, low-noise regime targeted by ground-based CMB experiments such as Atacama Cosmology Telescope (ACT) [2], South Pole Telescope (SPT) [3], Simons Observatory (SO) [4], and CMB-S4 [5]. This regime is dominated by ‘secondary’ CMB temperature anisotropies, which arise from interactions between CMB photons and large-scale structure (LSS) along the line of sight. The dominant blackbody component below arcminute angular scales is the kinetic Sunyaev Zel’dovich (kSZ) effect [6] - Thomson scattering of CMB photons from electrons in bulk motion. With existing CMB datasets, the kSZ effect has been detected at the $> 5\text{-}\sigma$ level using a variety of techniques, e.g. [7–10]. With future datasets from e.g. SO, the kSZ effect will be detected with far higher significance.

The kSZ effect is proportional to a line-of-sight integral over the product of the number density of free electrons and the locally observed CMB dipole projected along the line-of-sight - the remote dipole field. The kSZ effect is both a probe of astrophysics through the (inhomogeneous) number density of electrons as well as cosmology

through the remote dipole field. The astrophysical component of the kSZ effect is an important probe of the non-luminous ‘missing’ baryons in the Universe (e.g. [10–13]), however the focus here will be on the cosmological information contained in the remote dipole field.

The CMB dipole seen by an observer like us is primarily sourced by peculiar velocities in non-linear structure and has a magnitude of a few mK, corresponding to velocities of order $10^2 - 10^3$ km/s. This component has a correlation length of order the size of galaxy groups and clusters, extending to distances of up to ~ 50 Mpc. Coarse-graining on ~ 100 Mpc to Gpc scales, well into the linear regime, local velocities average down to the level of tens of km/s. On ultra-large scales, of order the cosmological horizon, the only contributions to the dipole are from last-scattering and the late-time Integrated Sachs-Wolfe effect, which are expected to be a few km/s in magnitude within ΛCDM . We refer to this component as the ‘primordial’ dipole ¹. The dipole field on these large scales has a correspondingly large correlation length of order Gpc. The remote dipole field sourcing the kSZ effect encodes both the local peculiar velocities as well as the primordial dipole, although the dominant component is from radial peculiar velocities. The remote dipole field can be an exquisite probe of the homogeneity of the Universe on the largest physical scales. New measurements on these scales can be used to probe e.g. large voids [14, 15], pre-inflationary relics [16], anomalies in the primary CMB anisotropies [17], primordial

¹ This component is also known as the ‘intrinsic’ dipole. It is the component of the CMB dipole that would be observed in the rest frame of the CMB, e.g. as defined by the frame with zero aberration of the temperature anisotropies.

* rbloch@my.yorku.ca

† mjohnson@perimeterinstitute.ca

non-Gaussianity [18–20], dark energy [21], modified gravity [22], and isocurvature [23, 24], among other scenarios.

In this paper we present a detailed analysis of a promising technique for extracting the remote dipole field: ‘kSZ tomography’ or ‘kSZ velocity reconstruction’ [25–30]. This technique utilizes the non-Gaussian information in the small angular-scale cross-correlation between the kSZ component of CMB temperature anisotropies and a tracer of LSS to reconstruct the remote dipole field on large angular scales. Given tracers at a variety of redshifts, a tomographic reconstruction of the remote dipole field along the past light cone is possible. The simplest implementation of kSZ velocity reconstruction, which we employ here, is the quadratic estimator first introduced in Ref. [27]². This quadratic estimator was validated using N-body simulations [29, 33], and the potential impact of foregrounds and systematics was assessed in Ref. [30]. This prior work forecasted a high signal to noise detection with near-term ground-based CMB experiments such as SO [4] and CMB-S4 [5] in combination with photometric or spectroscopic galaxy redshift surveys such as the Vera C. Rubin Observatory LSST [34] or DESI [35].

In preparation for this imminent flood of data, here we implement kSZ velocity reconstruction using existing data from the Planck CMB mission and galaxies from the Wide-Field Survey Infrared Explorer [36, 37] (WISE) assembled into the unWISE catalogue [38–41]. The Planck CMB temperature maps are well-characterized and provide a variety of ancillary datasets to assess the impact of foregrounds and instrumental systematics. The unWISE catalogue has $\sim 10^8$ objects split into three samples of increasing median redshift. Here, we focus on the ‘blue’ sample of Ref. [42] which has ~ 80 million objects over nearly the full sky. This dataset was chosen because large number densities and sky coverage are important for detecting the remote dipole field on large scales. This data combination has been used to detect the kSZ effect in Refs. [10, 12]. Previous work [30] forecasted a total signal to noise of order unity for kSZ velocity reconstruction within Λ CDM with this data combination. In the absence of a statistically significant detection, our focus here is on demonstrating that systematics and foregrounds can be controlled at the level of statistical reconstruction noise - we find that they can! This result demonstrates that the future is promising for kSZ velocity reconstruction.

We begin by tailoring the quadratic estimator introduced in Ref. [27] to surveys with wide photometric redshift bins. The unWISE blue sample has a broad redshift distribution spanning $0.2 \lesssim z \lesssim 1$. The quadratic estimator yields a single two-dimensional map that is a weighted average of the dipole field over the unWISE survey volume. A key element of the quadratic estimator is

the theoretical modelling of the galaxy-optical depth correlation function. If inaccurate, the estimator acquires a multiplicative ‘optical depth’ bias b_v . We demonstrate that photometric redshift uncertainties in the unWISE sample, uncertainties in the mean number density of electrons, and the degree of suppression of small-scale inhomogeneities in the electron distribution can in principle make significant contributions to the optical depth bias. We estimate that the optical depth bias can plausibly vary over the range $.5 \lesssim b_v \lesssim 1.1$. We include b_v as the only free parameter when comparing measurements to the expected remote dipole signal, fixing other cosmological parameters.

We then apply our estimator to individual frequency maps from Planck PR3 at 100, 143, 217, and 353 GHz to explore the impact of CMB foregrounds. We find that strong localized residuals in the reconstruction can be removed by masking. Correlations between unWISE and individual frequency maps in unmasked regions contribute primarily to the estimator monopole. This is consistent with the theoretical expectation [30] for a (nearly) statistically isotropic cross-correlation. After masking and removing the monopole and dipole, the reconstructions at all frequencies are consistent with the expected level of reconstruction noise from the primary CMB and instrumental noise only. This result demonstrates that even strong CMB foregrounds do not significantly impact the performance of the estimator.

Component-separated CMB maps in principle offer the highest signal-to-noise reconstruction available from Planck data. We apply our estimator to CMB maps produced using SMICA and Commander, which are based on qualitatively different techniques. Again, we find strong residuals mostly confined to regions falling within the unWISE mask. The estimator monopole has a far smaller magnitude than the individual frequency maps, indicating that statistically isotropic correlations from CMB foregrounds are greatly reduced, as expected. The reconstruction in both cases is consistent with theoretical expectations for the signal and reconstruction noise. Comparing the reconstructions, we see strong correlations for $\ell > 3$, with Commander displaying an uncorrelated excess power at lower ℓ . For our bottom-line CMB-unWISE reconstruction power spectrum, we use the cross-power between SMICA and Commander reconstructions.

Because they are sourced by the same underlying gravitational potentials, the signal component of the reconstruction is correlated with the unWISE galaxy density on large angular scales (for our model of unWISE, the correlation is significant for multipoles $\ell < 5$). Measuring this cross-power spectrum yields new information beyond the galaxy and estimator autospectra. The remote dipole (radial velocity) field on large angular scales is estimated from the small-scale CMB and unWISE maps, and therefore comes from independent data combinations. At a deeper level, the cross-correlation of the estimator with galaxy density is the squeezed limit of the galaxy-galaxy-temperature bispectrum. This data com-

² At high signal-to-noise, a maximum likelihood estimator is superior [31, 32].

bination is particularly interesting since it can be used to measure a scale-dependent bias induced by primordial non-Gaussianity [18–20] or isocurvature [23, 24]. We find that the measured cross-spectrum is consistent with the expected sample variance. This is significant in light of the fact that the unWISE autospectrum is dominated by large-angular scale systematic effects on multipoles $\ell \lesssim 20$, and provides strong evidence for the future success of kSZ velocity reconstruction as a probe of non-Gaussianity and isocurvature.

As a summary of the implications of our analysis for the remote dipole field, we compute the posterior over the optical depth bias b_v given the reconstruction. We find an upper limit of $b_v < 1.4$ at 68% confidence. This is consistent with our expectation that the total signal-to-noise of the reconstruction is order one for this data combination. In a companion paper [43] we use the reconstructed remote dipole field presented here to constrain a variety of cosmological models.

The paper is laid out as follows. In Sec. II we review kSZ velocity reconstruction and develop a quadratic estimator for large photometric redshift bins characterizing the unWISE sample. We outline the expected statistics for this estimator and possible sources of systematic error. In Sec. III we describe the properties of the datasets used as input for our reconstruction, various modelling assumptions implicit in the quadratic estimator, and predictions for the estimator response with these datasets. In Sec. IV we describe our analysis pipeline, and analyze reconstructions based on individual frequency and component-separated CMB maps. We characterize foregrounds, and constrain the cross-correlation of the reconstruction with unWISE galaxy density. In Sec. V we find the posterior probability distribution over the velocity bias b_v . We conclude and discuss the implications of our results in Sec. VI. We present a detailed assessment of the optical depth bias in Appendix A.

II. KSZ VELOCITY RECONSTRUCTION

We begin by reviewing how kSZ velocity reconstruction can be used to reconstruct the remote dipole field - the locally observed CMB dipole projected on our past light cone. For a more detailed discussion of kSZ velocity reconstruction/kSZ tomography, we refer the reader to Refs. [26–28, 30].

The kSZ contribution to the CMB temperature is a line-of-sight integral:

$$\Theta^{\text{kSZ}}(\hat{n}) = - \int d\chi \dot{\tau}(\hat{n}, \chi) v(\hat{n}, \chi) , \quad (1)$$

where $\dot{\tau}$ is the differential optical depth in direction \hat{n} at comoving distance χ , and v is the remote dipole field

defined by

$$v(\hat{n}, \chi) = \hat{n} \cdot \vec{v}(\hat{n}, \chi) + \sum_{m=-1}^1 v^m(\hat{n}, \chi) Y_{1m}(\hat{n}) , \quad (2)$$

$$v^m(\hat{n}, \chi) \equiv \int d^2\hat{n}' \Theta(\hat{n}, \chi, \hat{n}') Y_{1m}^*(\hat{n}') . \quad (3)$$

The first contribution is from the peculiar velocity $\vec{v}(\hat{n}, \chi)$ projected along the line of sight \hat{n} . This term is sourced by local density perturbations. The second contribution is the primordial dipole, the local CMB dipole observed at rest and determined by the CMB radiation field $\Theta(\hat{n}, \chi, \hat{n}')$. It receives contributions from the Sachs-Wolfe and integrated Sachs-Wolfe effects as well as Doppler shifts due to the velocity of plasma at last scattering. The primordial dipole directly probes the homogeneity of the Universe since it depends on the entirety of the surface of last scattering, not just the two-dimensional slice encoded in the primary CMB; for a detailed discussion see [26, 27].

Our focus here will be on cross-correlations with a photometric galaxy redshift survey, where the observed overdensity field is:

$$\delta^g(\hat{n}) = \int d\chi W_g(\chi) \delta^g(\hat{n}, \chi) , \quad (4)$$

where $\delta^g(\hat{n}, \chi)$ is the three-dimensional galaxy overdensity field and W_g is the galaxy window function defining the photometric sample.

The basis of kSZ velocity reconstruction is the statistically anisotropic cross-correlation between kSZ temperature anisotropies and a tracer of LSS. Schematically, the kSZ effect is a product of density and velocity, and therefore $\langle \delta^g \Theta^{\text{kSZ}} \rangle \sim \int d\chi \langle \delta^g \dot{\tau} v \rangle$. This three-point function is dominated by ‘squeezed’ configurations where velocity modes are far larger-scale than density modes [27, 28]. Therefore, the velocity field modulates small-scale power as $\langle \delta^g \Theta^{\text{kSZ}} \rangle \sim \int d\chi \langle \delta^g \dot{\tau} \rangle v$, and we can estimate the velocity from a quadratic estimator given by $\hat{v} \sim \delta^g \Theta / \int d\chi \langle \delta^g \dot{\tau} \rangle$. Given multiple photometric redshift bins, one can break-up the kSZ line-of-sight integral to perform a tomographic reconstruction of v .

Since we have no direct measurement of the optical depth, the quadratic estimator relies on a model for the (statistical) correlation between the LSS tracer and the optical depth as a function of redshift through $\int d\chi \langle \delta^g \dot{\tau} \rangle$. Mis-modelling this correlation leads to the ‘optical depth’ or ‘velocity’ bias (see e.g. [28, 44] for further discussion), which can be due to incorrect assumptions about the galaxy-halo connection and gas-halo connection, as well as poor characterization of the redshift distribution of the LSS tracer. Fortunately, previous work has demonstrated that the optical depth bias is scale-independent on large scales [30, 31, 33], and can therefore be described by a manageable number of nuisance parameters. We discuss the optical depth bias in detail in the analysis below.

A. Harmonic-space quadratic estimator

The quadratic estimator used in our analysis is based on off-diagonal correlations between CMB temperature and galaxy density in harmonic space:

$$\langle \Theta_{\ell m} \delta_{\ell' m'}^g \rangle = - \sum_{LM} w_{mm'-M}^{\ell \ell' L} \quad (5)$$

$$\times \int d\chi d\chi' [C_{\ell'}^{\tau g}(\chi, \chi')]^t v_{LM}(\chi) ,$$

where $[C_{\ell'}^{\tau g}(\chi, \chi')]^t$ is the true cross-power between the differential optical depth and galaxies on the past light cone and

$$w_{Mm_1-m}^{L\ell_1\ell} = (-1)^m \sqrt{\frac{(2L+1)(2\ell_1+1)(2\ell+1)}{4\pi}} \quad (6)$$

$$\times \begin{pmatrix} L & \ell_1 & \ell \\ M & m_1 & -m \end{pmatrix} \begin{pmatrix} L & \ell_1 & \ell \\ 0 & 0 & 0 \end{pmatrix} .$$

To make progress, we make two crucial assumptions. First, since most of the signal-to-noise in the reconstruction comes from density modes on small angular scales, we work in the Limber approximation. Next, we expand the galaxy-optical depth cross-power spectrum about some reference redshift $\chi = \bar{\chi}$ (typically the median redshift of the bin) and a reference scale $\ell = \bar{\ell}$ (typically $\bar{\ell} = 2 \times 10^3$; see discussion below). Defining $\bar{C}_{\ell'}^{\tau g} \equiv C_{\ell'}^{\tau g}(\chi = \bar{\chi}) \Delta\chi$ where $\Delta\chi$ is a normalization factor representative of the width of the redshift bin (defined more precisely below), we have

$$[C_{\ell'}^{\tau g}(\chi, \chi')]^t \simeq [C_{\ell'}^{\tau g}(\chi)]^t \delta(\chi' - \chi)$$

$$\simeq [\bar{C}_{\ell'}^{\tau g}]^t \frac{[C_{\ell=\bar{\ell}}^{\tau g}(\chi)]^t}{[\bar{C}_{\ell=\bar{\ell}}^{\tau g}]^t} \delta(\chi' - \chi) . \quad (7)$$

With these assumptions,

$$\langle \Theta_{\ell m} \delta_{\ell' m'}^g \rangle \simeq - \sum_{LM} w_{mm'-M}^{\ell \ell' L} [\bar{C}_{\ell'}^{\tau g}]^t \quad (8)$$

$$\times \int d\chi \frac{[C_{\ell=\bar{\ell}}^{\tau g}(\chi)]^t}{[\bar{C}_{\ell=\bar{\ell}}^{\tau g}]^t} v_{LM}(\chi) .$$

When this approximation is valid, the scale- and redshift-dependent factors in the cross-correlation can be separated.

Given Eq. (8) we can write down a simple quadratic estimator in analogy with those first presented in Refs. [27, 28, 30]:

$$\hat{v}_{\ell m} = -N_{\ell} \sum_{\ell_1 m_1; \ell_2 m_2} (-1)^m \begin{pmatrix} \ell_1 & \ell_2 & \ell \\ m_1 & m_2 & -m \end{pmatrix} \quad (9)$$

$$\times G_{\ell_1 \ell_2 \ell} \Theta_{\ell_1 m_1} \delta_{\ell_2 m_2} ,$$

where

$$N_{\ell} = (2\ell + 1) \left(\sum_{\ell_1 \ell_2} G_{\ell_1 \ell_2 \ell} f_{\ell_1 \ell_2 \ell} \right)^{-1} , \quad (10)$$

and (neglecting significant cross-correlations between the non-kSZ components of the CMB and the galaxy survey)

$$G_{\ell_1 \ell_2 \ell} \equiv \frac{f_{\ell_1 \ell_2 \ell}}{C_{\ell_1}^{\text{TT}} C_{\ell_2}^{\text{gg}}} . \quad (11)$$

C_{ℓ}^{TT} includes the primary CMB, instrumental noise, kSZ, as well as galactic and extragalactic foregrounds. C_{ℓ}^{gg} is the galaxy power spectrum including the clustering signal as well as shot noise and survey systematics. The CMB and galaxy power spectra are ideally based on self-consistent theoretical models; in practice it is acceptable to use the empirically measured power spectra of the input maps. The function $f_{\ell_1 \ell_2 \ell}$ is defined as:

$$f_{\ell_1 \ell_2 \ell} \equiv \sqrt{\frac{(2\ell_1+1)(2\ell_2+1)(2\ell+1)}{4\pi}} \begin{pmatrix} \ell_1 & \ell_2 & \ell \\ 0 & 0 & 0 \end{pmatrix} \bar{C}_{\ell_2}^{\tau g} , \quad (12)$$

where $\bar{C}_{\ell_2}^{\tau g}$ is a *model* for the galaxy-optical depth power spectrum (denoted by the absence of the ‘t’ superscript).

Computing the estimator mean, we find:

$$\langle \hat{v}_{\ell m} \rangle = \int d\chi W_v(\chi) v_{\ell m}(\chi) , \quad (13)$$

where

$$W_v(\chi) \equiv \frac{\sum_{\ell_1 \ell_2} G_{\ell_1 \ell_2 \ell} f_{\ell_1 \ell_2 \ell} [C_{\ell_2}^{\tau g}(\chi)]^t / \bar{C}_{\ell_2}^{\tau g}}{\sum_{\ell_1' \ell_2'} G_{\ell_1' \ell_2' \ell} f_{\ell_1' \ell_2' \ell}} . \quad (14)$$

The estimator variance is given by

$$\langle \hat{v}_{\ell m}^* \hat{v}_{\ell' m'} \rangle = C_{\ell}^{\hat{v} \hat{v}} \delta_{\ell \ell'} \delta_{m m'} \quad (15)$$

$$= \int d\chi d\chi' W_v(\chi) W_v(\chi') C_{\ell}^{v v}(\chi, \chi') \delta_{\ell \ell'} \delta_{m m'}$$

$$+ N_{\ell} \delta_{\ell \ell'} \delta_{m m'} .$$

Within Λ CDM the power spectrum for the remote dipole field is related to the primordial power spectrum $\mathcal{P}(k)$ by

$$C_{\ell}^{v v}(\chi, \chi') = \frac{2}{\pi} \int \frac{dk}{k} \Delta_{\ell}^v(k, \chi) \Delta_{\ell}^v(k, \chi') \mathcal{P}(k) . \quad (16)$$

The transfer function for the remote dipole field is

$$\Delta_{\ell}^v(k, \chi) = \frac{i^{\ell}}{2\ell+1} [S^{\text{LD}}(k, \chi) + S^{\text{P}}(k, \chi)]$$

$$\times [\ell j_{\ell-1}(k\chi) - (\ell+1) j_{\ell+1}(k\chi)] , \quad (17)$$

where $S^{\text{LD}}(k, \chi)$ is the ‘local Doppler’ source induced by the radial peculiar velocity field and $S^{\text{P}}(k, \chi)$ is the source for the ‘primordial’ dipole field induced by the Sachs-Wolfe, Integrated Sachs-Wolfe, and primordial Doppler components. The full form of the source functions can be found in Ref. [27].

Note that in general $W_v(\chi)$ is dependent on ℓ . However, this scale dependence is weak at low- ℓ (the case of interest below), and therefore we have suppressed the ℓ -dependence in the argument of this function. When

the ratio $[C_{\ell_2}^{\dot{\tau}g}(\chi)]^t / \bar{C}_{\ell_2}^{\tau g}$ is independent of ℓ_2 , the approximation in the second line of Eq. (7) is exact, and $W_v = [C_{\ell=\bar{\ell}}^{\dot{\tau}g}(\chi)]^t / \bar{C}_{\ell=\bar{\ell}}^{\tau g}$. We find below that this is an excellent approximation within our model. The velocity window function and estimator weights depend on $\bar{C}_{\ell_2}^{\tau g}$, which comes from a *model* for the galaxy-optical depth cross-correlation $C_{\ell_2}^{\dot{\tau}g}(\chi) \neq [C_{\ell_2}^{\tau g}(\chi)]^t$. We must incorporate this model uncertainty when comparing a reconstruction against theoretical expectations. We outline how a mis-match between the true and fiducial optical depth-galaxy cross-power contribute to the optical depth bias in Appendix A. Finally, we fix the normalization parameter $\Delta\chi$ by

$$\Delta\chi = \int d\chi C_{\ell=\bar{\ell}}^{\dot{\tau}g}(\chi) / C_{\ell=\bar{\ell}}^{\dot{\tau}g}(\chi = \bar{\chi}) , \quad (18)$$

given a model $C_{\ell_2}^{\dot{\tau}g}(\chi)$.

B. Pixel-space quadratic estimator

In the presence of incomplete sky coverage and masking, it is preferable to use a pixel-space form of the estimator in Eq. (9). This takes a particularly simple form when we neglect the scale dependence of N_ℓ defined in Eq. (10), which is an excellent approximation in the limit where $\ell_1, \ell_2 \gg \ell$ where :

$$N_\ell \simeq N \equiv \left[\sum_{\ell_1} \frac{2\ell_1 + 1}{4\pi} \frac{(\bar{C}_{\ell_1}^{\tau g})^2}{C_{\ell_1}^{TT} C_{\ell_1}^{gg}} \right]^{-1} . \quad (19)$$

We first define filtered CMB and galaxy fields:

$$\xi(\hat{n}) = \sum_{\ell m} \Theta_{\ell m} \frac{1}{C_{\ell}^{TT}} Y_{\ell m}(\hat{n}), \quad \zeta(\hat{n}) = \sum_{\ell m} \delta_{\ell m} \frac{\bar{C}_{\ell}^{\tau g}}{C_{\ell}^{gg}} Y_{\ell m}(\hat{n}) . \quad (20)$$

The filtering operation in $\xi(\hat{n})$ acts as a high-pass filter for the CMB, suppressing large-scale correlations. The filtering operation in $\zeta(\hat{n})$ will in general preserve fluctuations in the galaxy field on large scales where baryons and galaxies trace the underlying dark matter distribution, while suppressing power on scales ($\sim 1 - 10$ Mpc) affected by feedback processes. The pixel-space form of the quadratic estimator is

$$\hat{v}(\hat{n}) = -N \xi(\hat{n}) \zeta(\hat{n}) . \quad (21)$$

Due to the nature of the filtering, the product $\xi(\hat{n}) \zeta(\hat{n})$ is sensitive only to local correlations between the CMB and galaxy survey. This property is advantageous when dealing with masking and partial sky coverage.

The mean of the pixel-space estimator is

$$\langle \hat{v}(\hat{n}) \rangle = \int d\chi W_v(\chi) v(\hat{n}, \chi) , \quad (22)$$

which is consistent with Eq. (13). Turning to the pixel-space estimator variance, the contribution from the reconstruction noise deserves some discussion. Assuming that both $\xi(\hat{n})$ and $\zeta(\hat{n})$ are Gaussian random fields, the one-point function is a normal product distribution:

$$P(\hat{v}) = \frac{1}{\pi N \sigma_\xi \sigma_\zeta} K_0 \left[\frac{|\hat{v}|}{N \sigma_\xi \sigma_\zeta} \right] , \quad (23)$$

where $K_0(x)$ is the modified Bessel function of the second kind and

$$\begin{aligned} \sigma_\xi^2 &= \langle \xi(\hat{n})^2 \rangle \\ &= \sum_{\ell_1} \frac{2\ell_1 + 1}{4\pi} \frac{1}{C_{\ell_1}^{TT}} , \end{aligned} \quad (24)$$

and

$$\begin{aligned} \sigma_\zeta^2 &= \langle \zeta(\hat{n})^2 \rangle \\ &= \sum_{\ell_2} \frac{2\ell_2 + 1}{4\pi} \frac{(\bar{C}_{\ell_2}^{\tau g})^2}{C_{\ell_2}^{gg}} . \end{aligned} \quad (25)$$

The coincident two-point function is straightforward to compute from the one-point function:

$$\langle v(\hat{n})^2 \rangle = N^2 \sigma_\xi^2 \sigma_\zeta^2 . \quad (26)$$

To the extent that N_ℓ is independent of scale (which can be viewed as a consequence of the primarily local correlation of the filtered CMB and galaxy map), it is a reasonable approximation to neglect pixel-pixel correlations in the reconstruction noise. Upon coarse-graining, by the Central Limit Theorem, the distribution in coarse-grained pixels will be Gaussian. We can therefore treat reconstruction noise on large angular scales, where our signal lies, as Gaussian. However, retaining all scales, we speculate that the non-Gaussian properties of the reconstruction noise can be used as an additional method to distinguish it from the underlying Gaussian dipole field signal.

C. Possible sources of systematics

There are a number of potential systematic effects that could lead to a biased reconstruction. Previous work [29, 30] explored a variety of these effects using simulations, but the influence of systematics in an analysis of real data has not yet been performed - this is among the primary goals of this paper. Here, we present the expected systematics at a qualitative level.

In general, we can classify potential systematics into the following categories:

- **Optical depth bias:** When $C_{\ell_2}^{\dot{\tau}g}(\chi) \neq [C_{\ell_2}^{\tau g}(\chi)]^t$, the estimator mean will be biased against the true remote dipole field - referred to as the ‘optical depth’ or ‘velocity’ bias. This modelling error

can arise because of a poor understanding of the galaxy-halo and/or gas-halo connection, environmental/selection effects, and inaccurate/uncertain redshift distributions, among other factors arising from our limited knowledge of the distribution of baryons. Fortunately, so long as we focus on the reconstruction on large scales, this bias is scale independent [30, 33]. In Appendix A we estimate the possible magnitude of this bias by computing the expected signal over a range of model assumptions, finding that variations in the range $0.5 \lesssim b_v \lesssim 1.1$ are plausible.

- **Statistically isotropic CMB-galaxy cross-correlations:** An isotropic correlation between the CMB and galaxy survey, e.g. due to extragalactic CMB foregrounds such as the Cosmic Infrared Background (CIB) or thermal Sunyaev Zel'dovich effect (tSZ), contributes to the estimator weights. With a detailed model of the cross-correlation, this can be incorporated into $G_{\ell_1 \ell_2 \ell}$ defined in Eq. (11). Neglecting these contributions yields a slightly sub-optimal estimator (e.g. the variance is not as low as possible). Additionally, statistically isotropic correlations contribute to the monopole of the reconstruction, yielding an additive bias.
- **Statistically anisotropic CMB-galaxy cross-correlations:** The quadratic estimator in Eq. (9) is in principle sensitive to any effect that modulates the cross-correlation between the CMB and galaxies across the sky. Such effects lead to an additive bias. For example, given a signal in the CMB temperature $\Theta^M = M(\hat{n})\delta^M(\hat{n})$ where $\delta^M(\hat{n})$ is correlated with LSS, the mean estimator response is

$$\langle \hat{v}_{\ell m}^M \rangle = \frac{\sum_{\ell_1 \ell_2} G_{\ell_1 \ell_2 \ell} f_{\ell_1 \ell_2 \ell} C_{\ell_2}^{Mg}(\chi) / \bar{C}_{\ell_2}^{\tau g}}{\sum_{\ell'_1 \ell'_2} G_{\ell'_1 \ell'_2 \ell} f_{\ell'_1 \ell'_2 \ell}} M_{\ell m}. \quad (27)$$

This systematic can arise from physical effects such as CMB or galaxy lensing as well as relativistic effects modulating point source number counts (e.g. [45]). It can also arise from instrumental systematics such as anisotropic beams or anisotropic levels of foreground removal. Likewise, systematics and physical effects in the galaxy survey that modulate a component correlated with the CMB $\delta^P = P(\hat{n})\Theta^P(\hat{n})$ lead to a mean estimator response:

$$\langle \hat{v}_{\ell m}^P \rangle = \frac{\sum_{\ell_1 \ell_2} G_{\ell_1 \ell_2 \ell} f_{\ell_1 \ell_2 \ell} C_{\ell_2}^{PT}(\chi) / \bar{C}_{\ell_2}^{\tau g}}{\sum_{\ell'_1 \ell'_2} G_{\ell'_1 \ell'_2 \ell} f_{\ell'_1 \ell'_2 \ell}} P_{\ell m}. \quad (28)$$

A physical effect leading to this is the relativistic modulation of number counts. Systematic effects include extinction, redshift calibration errors, anisotropic depth, and background effects where e.g. the presence of nearby stars makes it difficult

to isolate extragalactic sources. A variety of potential foregrounds and systematics were considered in Ref. [30] and shown to make only small contributions to the estimator mean. Below, we evaluate the estimator response to templates for various physical and systematic effects.

- **Higher order noise bias:** There are additional contributions to the estimator variance presented in Eq. (15) beyond those we have considered here [33]. These arise from $\langle \Theta^{\text{kSZ}} \delta^g \Theta^{\text{kSZ}} \delta^g \rangle$. The disconnected components of this correlator are referred to, in analogy with CMB lensing, as the $N^{(1)}$ bias; the connected component due to non-linear clustering is referred to as the $N^{(3/2)}$ bias. These effects are only relevant in the high-signal-to-noise regime, and will not be discussed further here.

III. DATA AND THEORETICAL MODELLING

Before proceeding, we review the properties of ideal datasets for kSZ velocity reconstruction. The quadratic estimator relies on reconstructing the remote dipole field on large scales from anisotropic CMB-galaxy cross-power on small angular scales. The performance of the estimator therefore benefits from small-scale modes probed by a high resolution, low-noise CMB dataset and a galaxy survey that has a high number density of objects. Because the remote dipole field has power primarily on large angular scales, it is also desirable to have large sky coverage. In addition to these factors influencing the expected statistical error of the reconstruction, we must also worry about a variety of potential systematics, as described in the previous section. It is therefore desirable to utilize surveys with well-characterized foregrounds and instrumental systematics. Finally, it is desirable to have many redshift bins to perform a three-dimensional reconstruction of the dipole field along our past light cone.

In this paper, we use a data combination that has many of these desirable properties: Planck temperature anisotropies and galaxies from the unWISE ‘blue’ sample. The main shortcoming of this combination is the limited sensitivity of Planck and the lack of redshift resolution in the unWISE sample. We describe in this section the data products we utilize and our modelling assumptions.

A. Planck Temperature Maps

Our analysis utilizes temperature maps from the the Planck Data Release 3 (PR3) [1]. We analyze both individual frequency maps at 100, 143, 217, and 353 GHz as well as the SMICA [46] and Commander [47] component-separated CMB maps. In our assessment of various foregrounds and systematics, we additionally use a variety of CMB-subtracted maps and other ancillary Planck data

products. Here, we describe the relevant properties of these data products.

We perform an analysis using PR3 individual frequency maps at 100, 143, 217, and 353 GHz. Each of these frequency maps have a corresponding CMB-subtracted map for both SMICA and Commander estimates of the CMB, providing an estimate of the sum of all foregrounds and noise on the sky at each frequency. We apply the estimator to each of these maps to determine the influence of foregrounds on the reconstruction at each frequency. Individual frequency maps are deconvolved with a Gaussian beam of FWHM 9.68, 7.30, 5.02, and 4.94 arcminutes for 100, 143, 217, and 353 GHz frequencies respectively. We utilize simulated (galactic) foreground maps produced using the 10th Planck full focal plane simulation set (FFP10) [48] including free-free, synchrotron, and thermal dust components. We also utilize instrumental noise realizations from the FFP10 simulations.

For our 353 GHz analysis we employ the Planck-derived 353 GHz Cosmic Infrared Background (CIB) map of Ref. [49] to investigate the impact of CIB residuals on the reconstruction. These maps are provided alongside the window function intended for deconvolving these maps and we employ them as such.

We analyze maps produced using two different component separation techniques, SMICA and Commander, described in Ref. [46]. SMICA (Spectral Matching Independent Component Analysis) is based on a linear weighting of each Planck frequency map in harmonic space [50], such that the variance of a desired spectral component is minimized – here the blackbody spectrum, containing the primary CMB and kSZ. On the small angular scales relevant to the analysis presented below, the harmonic weights are largest in magnitude at 217, 353, and 857 GHz. Also of potential relevance to the discussion below, the SMICA map is itself a linear combination of two different harmonic linear combinations with weights relevant to foreground-free and sky-averaged regions. The Commander CMB map is determined by sampling from a posterior over a parametric model with a number of components. The amplitude and spectral indices of various components is allowed to vary over the sky. The resolution at which spectral indices are allowed to vary influences power on small angular scales [46]. Both CMB maps have an effective Gaussian beam with FWHM of 5 arcminutes, which we remove in our analysis; we work at the Planck native resolution of $N_{\text{side}} = 2048$.

B. unWISE Galaxy Map

The unWISE [41] catalogue contains over 500 million galaxies between $0 \leq z \leq 2$ constructed from NEOWISE data [36, 37]. unWISE provides among the largest currently available extragalactic catalogue with a measured redshift distribution, making it a desirable dataset for kSZ velocity reconstruction. Various catalogues derived from WISE data have already been successfully utilized

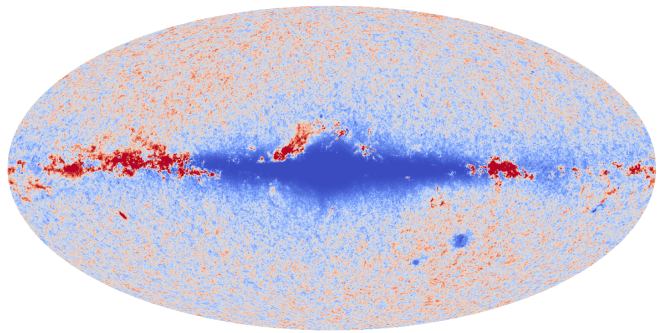


FIG. 1. The unWISE blue sample galaxy density. Small density fluctuations are shown with a linear color scaling and large density fluctuations are logarithmically scaled to enhance the cosmological signal compared with contaminants in the galactic plane.

in a wide variety of CMB cross-correlation studies including e.g. [10, 12, 13, 42, 51–58].

Here, we use the unWISE catalogue described in Ref. [42]. Objects in the full unWISE catalogue were cross-checked against Gaia DR2 [59] sources to reduce stellar contamination and divided into three large redshift bins labeled ‘red’, ‘green’, and ‘blue’ in order of descending median redshift. We focus on the blue sample for our analysis as it has the strongest confidence in redshift measurements and has the highest number density of galaxies. Future analyses could utilize all three samples to provide a true tomographic reconstruction of the remote dipole field.

In Fig. 1 we show the galaxy number density of the unWISE blue sample, defined from the number counts $N^g(\hat{n})$ by

$$\delta^g(\hat{n}) = (N^g(\hat{n}) - \bar{N}^g) / \bar{N}^g, \quad (29)$$

where $N^g(\hat{n})$ is the number of objects per pixel and the mean is defined by $\bar{N}^g \equiv N_{\text{tot}} / N_{\text{pix}}$ with N_{pix} the number of un-masked pixels at $N_{\text{side}} = 2048$ resolution and N_{tot} the total number of objects in un-masked pixels. For the unWISE blue sample with the mask defined in the following subsection, this is $\bar{N}^g = 2.8$, corresponding to a number density of 0.95 arcmin^{-2} . Visible in Fig. 1 are large over- and under-densities concentrated along the galactic plane. The clustering signal is visible far from the galactic plane.

C. Masking

To minimize the effect of a variety of galactic and extragalactic foregrounds in the Planck and unWISE maps, we employ a set of masks in our analysis. First, we must estimate the CMB power spectrum for use in the estimator weights. This computation is performed for individual frequency maps by applying the HFI point source mask and a galactic cut retaining 70% of the sky at 100

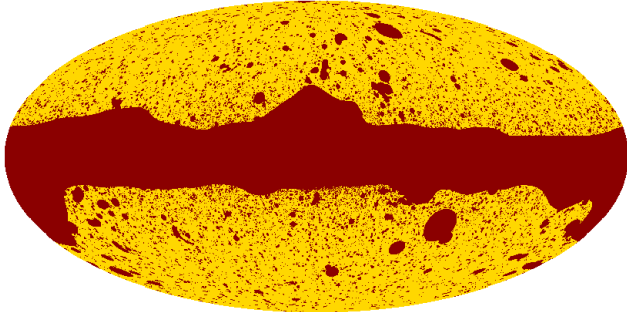
Fiducial Reconstruction Mask ($f_{\text{sky}} = 0.58$)

FIG. 2. The reconstruction mask applied to all reconstructions presented below. This mask is the union of the binary unWISE mask from [42] and the Planck CMB temperature confidence mask of Ref. [60]. The final uncut sky fraction for this mask is $f_{\text{sky}} = 0.58$.

GHz and 60% of the sky at 143, 217, and 353 GHz. Next, we estimate the galaxy power spectrum by applying the binary unWISE mask used in Ref. [42], composed of a galactic plane cut retaining 70% of the sky as well as masking of stars, planetary nebulae, and bright sources. The resulting mask has an uncut sky fraction of 58%. We also create a reconstruction mask which is the union of the unWISE mask and the SMICA-based confidence mask [60]. This mask, shown in Fig. 2, is applied to the final reconstructions to find power spectra. The sky coverage is nearly the same as the unWISE mask, also preserving 58% of the sky. For the analysis of the 353 GHz CIB map, we utilize the union of the unWISE mask and the mask of Ref. [49]. The resulting unmasked sky fraction is 18%.

D. Modelling assumptions

A necessary input to the quadratic estimator is the optical depth-galaxy cross-power spectrum; see Eq. (5). This is not currently measured from existing datasets (though it may be in the future, e.g. [61]), and so we must construct a model. Schematically, we connect unWISE galaxy number counts to electron density by modelling the relation of both to the underlying dark matter distribution.

A variety of previous works have attempted to constrain the relation between unWISE galaxies and dark matter, e.g. [10, 42, 53–56, 58]. We adopt the simplest linear-bias model used to model unWISE galaxies described in Ref. [42]. The galaxy power spectrum is:

$$C_\ell^{gg} = \int d\chi d\chi' W_g(\chi) W_g(\chi') C_\ell^{mm}(\chi, \chi') + N_{\text{shot}}, \quad (30)$$

where $C_\ell^{mm}(\chi, \chi')$ is the matter angular power spectrum

$$C_\ell^{mm}(\chi, \chi') = \frac{2}{\pi} \int \frac{dk}{k} \Delta_\ell^g(k, \chi) \Delta_\ell^g(k, \chi') \mathcal{P}(k), \quad (31)$$

with

$$\Delta_\ell^g(k, \chi) = S^m(k, \chi) j_\ell(k\chi), \quad (32)$$

where $S^m(k, \chi)$ is the source function for matter density. We neglect sub-dominant contributions from redshift space distortions and magnification that are relevant mostly on large angular scales. The shot noise for the unWISE blue sample is $N_{\text{shot}} = 9.2 \times 10^{-8}$ (steradians) and the galaxy window function W_g is defined by:

$$W_g(\chi) \equiv b_g(z) \frac{dN}{dz} H(z), \quad b_g(z) \equiv 0.8 + 1.2z. \quad (33)$$

Here, $b_g(z)$ is the galaxy bias and dN/dz is the redshift distribution; both were empirically determined for the unWISE blue sample in Ref. [42]. The redshift distribution dN/dz was determined from matching sources with deep photometric redshifts in COSMOS [62]; the galaxy bias $b(z)$ was determined through cross-correlation with SDSS spectroscopic galaxies in narrow bins. Note that some other works [53, 54, 56] using the unWISE catalogue are based on a measurement of the product of galaxy bias and the redshift distribution from cross-correlation with SDSS alone. Within our model, the clustering signal dominates over shot noise for $\ell \lesssim 10^3$. In the limber approximation, the galaxy-galaxy power spectrum in this model is:

$$C_\ell^{gg} = \int \frac{d\chi}{\chi^2} P_{mm} \left(\chi, k = \frac{\ell + \frac{1}{2}}{\chi} \right) W_g^2(\chi) + N_{\text{shot}}, \quad (34)$$

where P_{mm} is the non-linear matter power spectrum computed using CAMB. The Limber approximation is accurate on scales $\ell \gtrsim 100$ for this model.

Uncertainty in the redshift distribution $\frac{dN}{dz}$ for the unWISE blue sample is an important systematic in our analysis. In Ref. [42] this was quantified by determining the variance in the redshift distribution over 44 different patches observed by HSC, each with the same area as COSMOS, and then drawing 100 samples consistent with this expected error. The 100 $\frac{dN}{dz}$ realizations used in Ref. [42] are shown in Fig. 3 as thin grey lines, with the thick red line indicating the best-fit fiducial $\frac{dN}{dz}$. This spread illustrates the degree of uncertainty in the unWISE blue redshift distribution, and will be important in the discussion below.

The differential optical depth is proportional to the inhomogeneous distributions of electrons. We relate this to the dark matter distribution through a scale-dependent linear bias $\delta_e(\vec{k}, \chi) = b_e(k, \chi) \delta_m(\vec{k}, \chi)$, employing the model of Ref. [63]:

$$b_e(z, k) = b_*(z) \left[1 + \left(\frac{k}{k_*(z)} \right)^{\gamma(z)} \right]^{-\frac{1}{2}}, \quad (35)$$

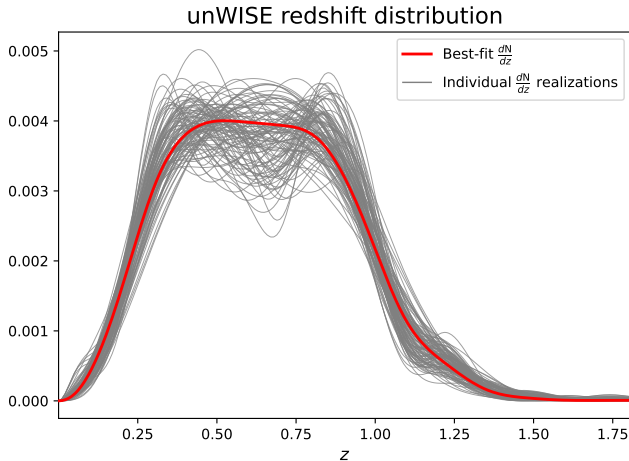


FIG. 3. Normalized redshift distribution $\frac{dN}{dz}$ for the unWISE blue sample. The thin grey lines are 100 individual samples of $\frac{dN}{dz}$ consistent with the expected error. The thick red line indicates the measured $\frac{dN}{dz}$, taken to be the fiducial redshift distribution used in our analysis.

where

$$\begin{aligned} b_*(z) &= \sqrt{-0.013z + 0.971} , \\ \gamma(z) &= 0.10z^2 - 0.59z + 1.91 , \\ k_*(z) &= -0.42z^3 + 3.10z^2 - 3.24z + 4.36 . \end{aligned} \quad (36)$$

Heuristically, b_* controls the redshift-dependence of the amplitude, k_* controls the scale on which electron inhomogeneities are suppressed as compared to dark matter, and γ controls the abruptness of this transition.

In the Limber approximation, the cross-power is

$$\begin{aligned} C_{\ell}^{\tau g}(\chi) &= \frac{1}{\chi^2} W_g(\chi) W_{\tau}(\chi) b_e\left(\chi, k = \frac{\ell + \frac{1}{2}}{\chi}\right) \\ &\times P_{mm}\left(\chi, k = \frac{\ell + \frac{1}{2}}{\chi}\right) . \end{aligned} \quad (37)$$

W_{τ} is the optical depth window function:

$$W_{\tau}(\chi) \equiv \sigma_T \bar{n}_{e,0} (1 + z(\chi))^2 , \quad (38)$$

where σ_T is the Thomson cross section, $a(\chi)$ is the scale factor, and $\bar{n}_{e,0}$ is the average number density of electrons today. We model $\bar{n}_{e,0}$ as

$$\bar{n}_{e,0} = \frac{f_{\text{gas}} X \Omega_{b,0} \rho_{\text{crit},0}}{\mu_e m_p} , \quad (39)$$

where f_{gas} is the mass fraction of baryons in ionized gas, X is the fraction of the total number of electrons that are ionized, $\mu_e m_p$ is the mean baryon mass per electron, $\Omega_{b,0}$ is the present-day baryon density parameter, and $\rho_{\text{crit},0}$ is the present-day critical density. Assuming a primordial helium abundance of $Y_p = 0.24$, and assuming that all helium is doubly ionized within the redshifts

probed by unWISE (helium reionization is expected to have happened at $z \gtrsim 2.5$ near the peak of quasar activity [64–70]), we have $X = 1^3$ and $\mu_e = 1.14$. We assume that 10% of baryonic matter by mass is cold (neutral) or bound up in stars, yielding $f_{\text{gas}} = 0.9$. We do not consider redshift-evolution of the ionization state of Helium in the intergalactic medium or the ionized gas fraction over cosmological epochs probed by the unWISE blue sample⁴. With our fiducial cosmological parameters, we have $\sigma_T \bar{n}_{e,0} \simeq 4.08 \times 10^{-7} \text{ Mpc}^{-1}$.

Uncertainty in the distribution of electrons, here quantified by the scale-dependent bias $b_e(z, k)$, is an important systematic to consider. Within our assumed model, the bias is close to unity on large physical/angular scales, where baryons trace the underlying distribution of dark matter. Various feedback effects become relevant on physical scales $k > k_*$, washing out baryon fluctuations; this is modelled through a decrease in $b_e(z, k)$. At the median redshift of the unWISE blue sample $\bar{z} \simeq 0.6$, this transition corresponds to physical scales $k \sim 1 \text{ Mpc}^{-1}$ and angular scales $\ell \gtrsim k\chi \sim 2300$. At this angular scale there is still significant signal-to-noise in the Planck CMB and the clustering signal in unWISE, implying that there will be some sensitivity to variations about the fiducial model. In Appendix A we quantify the impact of varying the model parameters in $b_e(z, k)$ on the optical depth bias b_v .

As described in Sec. II, the estimator mean has the simplest interpretation when we can factorize the scale- and redshift-dependence of the optical depth-galaxy cross-power. This allows us to approximate $C_{\ell}^{\tau g}(\chi) \simeq \bar{C}_{\ell}^{\tau g} (C_{\ell=\bar{\ell}}^{\tau g}(\chi) / \bar{C}_{\ell=\bar{\ell}}^{\tau g})$ on small angular scales where the estimator receives the greatest contributions. Within our model, we can re-state this as testing the approximation

$$\frac{P_{me}\left(\chi, k = \frac{\ell+1/2}{\chi}\right)}{P_{me}\left(\chi, k = \frac{\bar{\ell}+1/2}{\chi}\right)} \simeq \frac{P_{me}\left(\bar{\chi}, k = \frac{\ell+1/2}{\bar{\chi}}\right)}{P_{me}\left(\bar{\chi}, k = \frac{\bar{\ell}+1/2}{\bar{\chi}}\right)} . \quad (41)$$

For our fiducial model, we find that this approximation is better than 90% accurate over the full range of scales at redshifts near $\bar{\chi}$, and at worst 70% accurate on small angular scales in the tails of the unWISE blue sample redshift distribution. This validates the intuition behind our construction of the estimator. In Fig. 4 we plot the velocity window function computed using the approximate expression $W_v \simeq C_{\ell=\bar{\ell}}^{\tau g}(\chi) / \bar{C}_{\ell=\bar{\ell}}^{\tau g}$ (blue) against the

³ The fraction of ionized electrons is defined as

$$X \equiv \frac{1 - Y_p(1 - N_{\text{He}}/4)}{1 - Y_p/2} , \quad (40)$$

where $N_{\text{He}} = 0, 1, 2$ for neutral, singly-ionized, and doubly-ionized helium. For a primordial helium abundance of $Y_p = 0.24$, this takes values $X = 0.86, 0.93, 1.0$ for these three ionization states, respectively.

⁴ With future surveys covering a broader range of redshifts, it will be possible to measure Helium reionization using kSZ tomography [71–73].

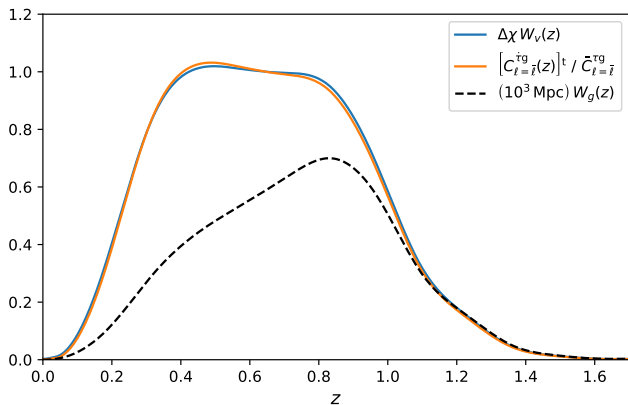


FIG. 4. The velocity window function $W_v(z)$ Eq. (14) (blue solid) relating the estimator mean to the underlying velocities, the approximate window function used in our analysis (orange), and the galaxy window function $W_g(z)$ Eq. (33).

exact expression Eq. (14) (orange). The agreement is excellent. The distribution is relatively flat over the redshift range $0.3 \lesssim z \lesssim 0.9$, and covers the same redshift range as the galaxy window function (which we plot for comparison, dashed black), albeit with a different shape.

E. Predicted estimator variance

We now have everything necessary to compute the estimator variance defined in Eq. (15). We can estimate the expected level of reconstruction noise from Eq. (19) using the fiducial model for $C_\ell^{\tau g}$ and C_ℓ^{gg} described above and estimating C_ℓ^{TT} as the sum of the primary CMB and an effective white noise level of 77.4, 33.0, 46.8, 153.6 $\mu\text{K-arcmin}$ for the 100, 143, 217, and 353 GHz channels respectively. In Fig. 5 we show the resulting summand in Eq. (19). The larger the summand, the smaller the reconstruction noise. The multipoles over which the summand is significant determines which scales contribute most to the estimator variance. From this plot, we see that the 217 GHz map is expected to yield the lowest reconstruction noise (before incorporating foregrounds) and that scales $\ell \simeq 2000$ are most relevant to the reconstruction. This motivates our choice of $\bar{\ell} = 2000$ as the reference scale for our model of the galaxy-optical depth power spectrum.

We compare the reconstruction noise expected for the 217 GHz Planck map against the expected signal contributions in Fig. 6. The reconstruction noise computed as described above (black solid) is comparable to the total predicted signal (red solid, computed using Eq. (15) with the fiducial velocity window function shown in Fig. 4) at the very lowest ℓ , falling steeply on smaller scales. The primordial component (green dashed; computed using the primordial dipole source term in Eq. (17)) does not significantly contribute to the predicted signal for this

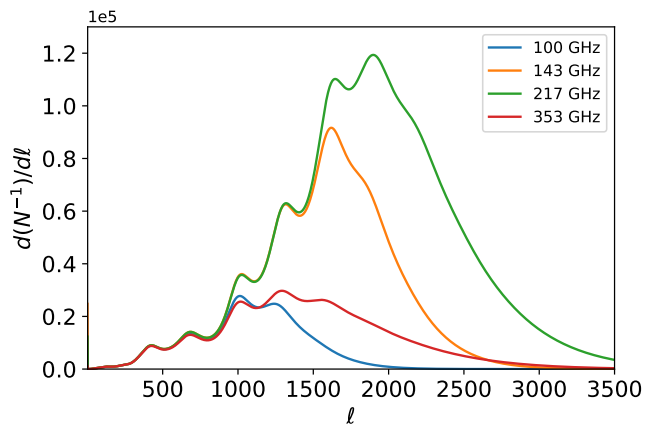


FIG. 5. The predicted summand in Eq. (19) for reconstructions from individual frequency maps. The range in ℓ where the summand is largest determines the scales that make the largest contribution to the estimator variance.

data combination ⁵. The expected total signal-to-noise of the map-level reconstruction defined as:

$$\text{SN}^2 = \sum_{\ell} \frac{2\ell + 1}{2} f_{\text{sky}} \left(\frac{C_{\ell}^{vv}}{N_{\ell}} \right)^2, \quad (42)$$

is $\text{SN} = 0.89$, with most of the contribution coming from $\ell < 5$ (and roughly half from $\ell = 1$). Note that incorporating the mask as a factor of f_{sky} is likely inaccurate at such large angular scales (see e.g. Ref. [75] for a related discussion). Additionally, this forecast does not incorporate any degradation from foregrounds and systematics. Therefore, we do not anticipate a conclusive detection for this data combination within ΛCDM . Note however that the statistical reach of the quadratic estimator for bulk radial velocities on Gpc scales is an impressive $\sqrt{N} \sim 25 \text{ km/s}$! Future CMB experiments such as Simons Observatory have the statistical power to achieve $\text{SN} > 5$ in cross-correlation with the unWISE blue sample (and $\text{SN} > 100$ in combination with LSST) [30]; detection of the primordial dipole signal likely requires both CMB-S4 and LSST [19].

F. Optical depth bias

Uncertainties in the modelling choices used to construct $C_{\ell}^{\tau g}$ appear as a bias on the estimator mean and variance, known as the optical depth bias (see Sec. II C). We present a detailed computation and assessment of the optical depth bias in Appendix A, collecting the

⁵ The suppression of power at $\ell = 1$ is due to the cancellation of contributions to the locally observed CMB dipole that occurs for long-wavelength adiabatic modes. See Refs. [26, 74] for a detailed discussion.

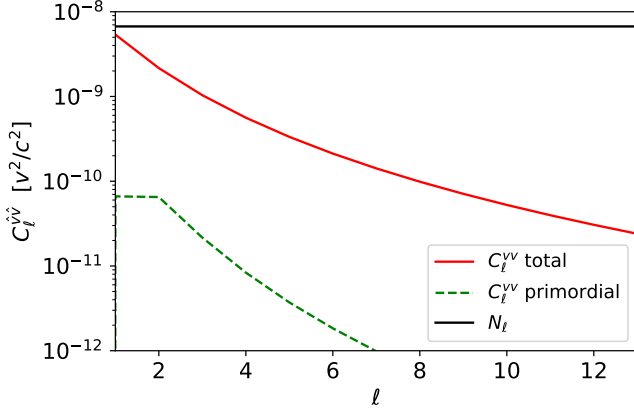


FIG. 6. The predicted signal and noise power spectra for the reconstructed remote dipole field. The full remote dipole spectrum (red solid) is several orders of magnitude larger than the spectrum associated with the primordial dipole (green dashed); see Eq. (17). The expected reconstruction noise for the 217 GHz map (black solid) is comparable to the expected signal on the largest angular scales.

main results here. In general, we can define the optical depth bias by the estimator mean evaluated using the true temperature-galaxy cross-correlation, but with fiducial estimator weights:

$$\langle \hat{v}_{\ell m} \rangle^t = \int d\chi b_v(\chi) W_v(\chi) v_{\ell m}(\chi), \quad (43)$$

where the ‘t’ superscript indicates this is evaluated on the ‘truth’ values for the temperature-galaxy cross-correlation. In Appendix A, we demonstrate that this can be approximated by

$$b_v(\chi) \simeq \frac{\sum_{\ell_1} \frac{2\ell_1+1}{4\pi} \frac{\bar{C}_{\ell_1}^{\tau g} [\bar{C}_{\ell_1}^{\tau g}]^t}{C_{\ell_1}^{\tau\tau} C_{\ell_1}^{\tau g}} [C_{\ell=\bar{\ell}}^{\tau g}(\chi)]^t \bar{C}_{\ell=\bar{\ell}}^{\tau g}}{\sum_{\ell_2} \frac{2\ell_2+1}{4\pi} \frac{(\bar{C}_{\ell_2}^{\tau g})^2}{C_{\ell_2}^{\tau\tau} C_{\ell_2}^{\tau g}} C_{\ell=\bar{\ell}}^{\tau g}(\chi) [\bar{C}_{\ell=\bar{\ell}}^{\tau g}]^t} \quad (44)$$

Given a range of possible models for the ‘truth,’ we can assess the range of b_v we might plausibly expect. Note that in general the optical depth bias is a χ -dependent function. However, on large angular scales it manifests as a multiplicative constant relating the reconstruction and the true velocity. We define b_v without the explicit χ dependence as this constant multiplicative factor:

$$\langle \hat{v}_{\ell m} \rangle^t \simeq b_v \langle v_{\ell m} \rangle, \quad [C_{\ell}^{\hat{v}\hat{v}}]^t \simeq b_v^2 C_{\ell}^{\hat{v}\hat{v}}. \quad (45)$$

Note that the reconstruction noise N is defined by the fiducial model in the estimator, so using the reconstruction noise to place limits on any hypothetical underlying signal requires an understanding of b_v . For example, the total expected signal-to-noise defined in Eq. (42) scales as $[SN]^t \simeq b_v^2 SN$.

In Appendix A we estimate the range of values that b_v could plausibly take by varying the unWISE photometric

redshift distribution (see Fig. 3), the model parameters determining b_e , and the mean number density of electrons. We find that all three of these uncertainties can contribute to the optical depth bias at the $\mathcal{O}(10\%)$ -level. Under the variations we consider, we find that it is difficult to increase b_v beyond $b_v \sim 1.1$. Under the largest variations we consider in the scale and abruptness of electron power suppression determining b_e , we can obtain values of b_v as small as $b_v \sim 0.5$. Under the assumption that our model is flexible enough to encompass the true underlying spectrum, we can plausibly expect that b_v lies in the range $0.5 \lesssim b_v \lesssim 1.1$. Although we do not pursue it here, we note that it is in principle possible to derive a prior on b_v using a variety of measurements and upper-limits on e.g. the kSZ power spectrum [76], pairwise velocity [7] or projected field [10, 12, 13] kSZ estimators, numerical simulations including baryonic feedback, etc. Future analyses with more precisely calibrated photometric or spectroscopic redshifts will also mitigate the optical depth bias.

G. Galaxy-reconstruction cross-correlation

The reconstructed remote dipole field is correlated with the galaxy density on large angular scales. This cross-correlation is equivalent to the squeezed limit of the temperature-galaxy-galaxy bispectrum [28] (e.g. $\langle T_S \delta_S^g \delta_L^g \rangle$) where S denotes small angular scales and L denotes large angular scales). We can estimate the predicted signal from our theoretical models for the estimator mean and the galaxy density

$$C_{\ell}^{\hat{v}g} = \int d\chi \int d\chi' W_v(\chi) W_g(\chi') C_{\ell}^{vg}(\chi, \chi'). \quad (46)$$

The galaxy-velocity cross-correlation is

$$C_{\ell}^{vg}(\chi, \chi') = \frac{2}{\pi} \int \frac{dk}{k} \Delta_{\ell}^v(k, \chi) \Delta_{\ell}^g(k, \chi') \mathcal{P}(k), \quad (47)$$

where Δ_{ℓ}^v and Δ_{ℓ}^g are defined in Eq. (17) and (32) respectively. This is shown in Fig. 7. There is a significant positive correlation for $\ell < 5$, and a slowly decreasing anti-correlation for $\ell > 10$. The expected variance on the cross-spectrum based on the theoretical model for the galaxy power spectrum and remote dipole estimator variance is

$$\langle (C_{\ell}^{\hat{v}g})^2 \rangle = \frac{C_{\ell}^{gg} C_{\ell}^{\hat{v}\hat{v}}}{2\ell + 1}. \quad (48)$$

We discuss this in detail in the next subsection. The variance is roughly twice the expected signal at $\ell = 1$ and more than an order of magnitude larger at $\ell \sim 10$, with the ratio growing roughly linearly with ℓ thereafter. We therefore do not expect a detection of the signal in the cross-power.

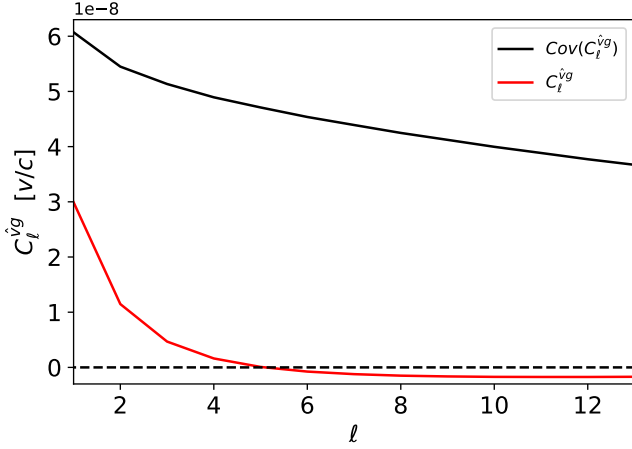


FIG. 7. The predicted cross-correlation between the galaxy density and estimator mean (red solid; see Eq. (46)) and the expected covariance based on the theoretical reconstruction and galaxy auto spectra (black solid; see Eq. 48).

H. Likelihood and posterior

Assuming that the reconstructed dipole field and unWISE galaxy density are Gaussian random fields (a good approximation on large angular scales), the likelihood for the observed spectra $\hat{\mathbf{C}}_\ell$ given theory spectra \mathbf{C}_ℓ is at each ℓ given by a Wishart distribution:

$$p(\hat{\mathbf{C}}_\ell | \mathbf{C}_\ell) \propto \frac{[\det(\hat{\mathbf{C}}_\ell)]^{(\nu-3)/2}}{[\det(\mathbf{C}_\ell)]^{\nu/2}} \times \exp\left[-\frac{\nu}{2} \text{Tr}(\mathbf{C}_\ell^{-1} \cdot \hat{\mathbf{C}}_\ell)\right], \quad (49)$$

where $\nu \equiv 2\ell + 1$, the measured spectra are assembled into the matrix

$$\hat{\mathbf{C}}_\ell = \begin{pmatrix} \hat{C}_\ell^{\hat{v}\hat{v}} & \hat{C}_\ell^{\hat{v}g} \\ \hat{C}_\ell^{\hat{v}g} & \hat{C}_\ell^{gg} \end{pmatrix}, \quad (50)$$

and the theory spectra are assembled into

$$\mathbf{C}_\ell = \begin{pmatrix} C_\ell^{\hat{v}\hat{v}} & C_\ell^{\hat{v}g} \\ C_\ell^{\hat{v}g} & C_\ell^{gg} \end{pmatrix}. \quad (51)$$

For large- ℓ , the Wishart distribution approaches a multivariate Gaussian distribution over the spectra. By marginalizing over \hat{C}_ℓ^{gg} and $\hat{C}_\ell^{\hat{v}g}$ (e.g. discluding these observables from our data vector) we obtain the likelihood for $\hat{C}_\ell^{\hat{v}\hat{v}}$ which is a Gamma function:

$$p(\hat{C}_\ell^{\hat{v}\hat{v}} | C_\ell^{\hat{v}\hat{v}}) = \left(\frac{\nu}{2}\right)^{\nu/2} \frac{(\hat{C}_\ell^{\hat{v}\hat{v}})^{\nu/2-1}}{2^{\nu/2} \Gamma(\nu/2)} \exp\left[-\frac{\nu \hat{C}_\ell^{\hat{v}\hat{v}}}{2 C_\ell^{\hat{v}\hat{v}}}\right]. \quad (52)$$

The mean is $C_\ell^{\hat{v}\hat{v}}$ and the variance $2C_\ell^{\hat{v}\hat{v}2}/\nu$; at high ℓ this approaches a Gaussian with this mean and variance. We

will also be interested below in the likelihood over $\hat{C}_\ell^{\hat{v}g}$ given a set of theory spectra. Marginalizing Eq. (49) over $\hat{C}_\ell^{\hat{v}\hat{v}}$ and \hat{C}_ℓ^{gg} we have

$$p(\hat{C}_\ell^{\hat{v}g} | \mathbf{C}_\ell) = \frac{\nu 2^{(1-\nu)/2}}{\sqrt{\pi} \Gamma(\nu/2) [\det(\mathbf{C}_\ell)]^{1/2}} \left[\frac{(\nu \hat{C}_\ell^{\hat{v}g})^2}{C_\ell^{\hat{v}\hat{v}} C_\ell^{gg}} \right]^{(\nu-1)/4} \times \exp\left[\frac{\nu \hat{C}_\ell^{\hat{v}g} C_\ell^{\hat{v}g}}{\det(\mathbf{C}_\ell)} \right] K_{\nu/2-1} \left[\frac{\nu |\hat{C}_\ell^{\hat{v}g}| \sqrt{C_\ell^{\hat{v}\hat{v}} C_\ell^{gg}}}{\det(\mathbf{C}_\ell)} \right]. \quad (53)$$

The mean is $C_\ell^{\hat{v}g}$ and the variance for small $C_\ell^{\hat{v}g}$ is approximately equal to $C_\ell^{\hat{v}\hat{v}} C_\ell^{gg} / \nu$; at high ℓ this approaches a Gaussian with this mean and variance.

On the full sky, the spectra at different multipoles ℓ are independent, and the joint likelihood for the full spectrum can be constructed by simply multiplying the likelihood at each ℓ :

$$p(\hat{\mathbf{C}} | \mathbf{C}) \propto \prod_{\ell=\ell_{\min}}^{\ell_{\max}} p(\hat{\mathbf{C}}_\ell | \mathbf{C}_\ell). \quad (54)$$

Below, we must introduce sky cuts to mitigate foreground contamination in the reconstruction and unWISE galaxy density. We can employ the likelihood functions described above if we have an estimate for the full-sky spectra $\hat{\mathbf{C}}_\ell$ from the pseudo- C_ℓ spectra we measure on the cut-sky. We expect the measured dipole field to be dominated by reconstruction noise, with a flat angular power spectrum. In this special case, a good approximation to the full-sky power spectrum can be obtained by simply dividing the measured pseudo- C_ℓ spectra by a factor of f_{sky} . We assume this is the case in our analysis and defer a more careful implementation of power spectrum estimation to future work.

Below, we consider variations in the velocity bias, employing the model

$$C_\ell^{\hat{v}\hat{v}} = b_v^2 C_\ell^{vv} + N. \quad (55)$$

We fix the reconstruction noise N as well as all cosmological parameters determining C_ℓ^{vv} . The velocity bias b_v encodes the uncertainty in the galaxy-optical depth cross-power. Assuming a flat prior on the model spectra, we can use the measured spectra $\hat{C}_\ell^{\hat{v}\hat{v}}$ to obtain the posterior distribution over b_v :

$$p(b_v | \hat{C}_\ell^{\hat{v}\hat{v}}) \propto \prod_{\ell=\ell_{\min}}^{\ell_{\max}} p(\hat{C}_\ell^{\hat{v}\hat{v}} | C_\ell^{\hat{v}\hat{v}}(b_v)), \quad (56)$$

where the likelihood function $p(\hat{C}_\ell^{\hat{v}\hat{v}} | C_\ell^{\hat{v}\hat{v}}(b_v))$ defined in Eq. (52) is evaluated over $0 < b_v < \infty$; normalizing the distribution over b_v , we obtain the posterior.

IV. RESULTS

We now proceed to describe our analysis using Planck individual frequency and component-separated maps and

the unWISE blue sample number counts. We begin by describing the analysis pipeline. We then present the dipole field reconstruction based on individual frequency maps, and investigate the impact of various foregrounds and systematics, followed by an analysis of reconstructions based on the SMICA and Commander CMB maps. Finally, we measure the cross-correlation of the reconstruction and unWISE galaxy density on large angular scales.

A. Analysis pipeline

The analysis pipeline proceeds as follows:

1. **Compute input spectra:** We first pre-compute the various quantities necessary to construct the estimator. The galaxy-optical depth cross-power $\bar{C}_\ell^{\tau g}$ is computed from the model (Eq. (37)) evaluated at the reference redshift $\bar{z} = 0.68$, corresponding to $\bar{\chi} = 2505$ Mpc. Where spectra are computed at a reference multipole, we use $\bar{\ell} = 2000$. We estimate C_ℓ^{TT} by computing the power spectrum of the masked temperature map, re-scaling by f_{sky}^{-1} and dividing by a Gaussian beam of the appropriate width: $C_\ell^{TT} = [C_\ell^{TT}]^{\text{masked map}} / f_{\text{sky}} / B_\ell(\theta_{\text{FWHM}})^2$. The choices of mask, f_{sky} , and θ_{FWHM} used in our analysis are recorded in Table I. This spectrum is used in the estimator normalization (Eq. (19)) and in the inverse-variance filtering operation (Eq. (20)). We then estimate the unWISE blue galaxy power spectrum by computing the power spectrum of the masked unWISE blue number density map re-scaled by f_{sky} : $C_\ell^{gg} = [C_\ell^{gg}]^{\text{masked map}} / f_{\text{sky}}$. We use the unWISE mask described in Sec. III C, with $f_{\text{sky}} = 0.58$. The power spectra described above are used to compute the estimator normalization in Eq. (19).
2. **Filter:** The inputs to the pixel-space quadratic estimator are the filtered CMB field $\xi(\hat{n})$ and galaxy field $\zeta(\hat{n})$ defined in Eq. (20). To construct $\xi(\hat{n})$ we perform a forward spherical harmonic transform of the unmasked maps at healpix resolution $N_{\text{side}} = 2048$. We then apply a high- and low-pass filter that nulls all harmonic coefficients $\ell < 100$ and $\ell > 4000$. From Fig. 5 this range of scales should include all significant contributions to the estimator variance, while mitigating the impact of foregrounds and systematics on very large and very small angular scales. We divide by the power spectrum C_ℓ^{TT} computed as described above, which is representative of the expected CMB power in un-masked regions of the sky. We then perform an inverse spherical harmonic transform to obtain $\xi(\hat{n})$. To construct $\zeta(\hat{n})$ we perform a forward spherical harmonic transform of the unmasked unWISE blue number density map at healpix resolution $N_{\text{side}} = 2048$. We then apply a high- and

Temperature Map	Mask	f_{sky}	θ_{FWHM}
100 GHz	Pt Src & 70% Gal	0.696	9.68
143 GHz	Pt Src & 60% Gal	0.598	7.30
217 GHz	Pt Src & 60% Gal	0.598	5.02
353 GHz	Pt Src & 60% Gal	0.598	4.94
SMICA	CMB	0.779	5.0
Commander	CMB	0.779	5.0

TABLE I. Analysis choices for estimating the CMB temperature autospectrum through $C_\ell^{TT} = [C_\ell^{TT}]^{\text{masked map}} / f_{\text{sky}} / B_\ell(\theta_{\text{FWHM}})^2$. This quantity is used in Eq. (19) and (20). Pt Src refers to the PR3 HFI point source mask at the corresponding frequency, Gal refers to the PR3 HFI galactic mask, and CMB refers to the PR3 common CMB mask.

low-pass filter that nulls all harmonic coefficients $\ell < 100$ and $\ell > 4000$. We filter in harmonic space by the ratio $\bar{C}_\ell^{\tau g} / C_\ell^{gg}$ where $\bar{C}_\ell^{\tau g}$ and C_ℓ^{gg} are computed as described above. We inverse spherical harmonic transform to obtain $\zeta(\hat{n})$.

3. **Assemble and analyze the reconstruction:** The quadratic estimator for the dipole field Eq. (21) is simply the product of the $\xi(\hat{n})$ and $\zeta(\hat{n})$ maps at full resolution of $N_{\text{side}} = 2048$, rescaled by N defined in Eq. (19). For visualization purposes, below we filter maps with a Gaussian kernel of width $\sigma_{\text{FWHM}} = 10^\circ$. For analysis, we apply the reconstruction mask described in Sec. III C with $f_{\text{sky}} = 0.58$, and then estimate/remove the monopole and dipole from the unmasked pixels (using the healpix function `fit_dipole`).

This analysis pipeline is followed to produce a total of 6 reconstructions of the remote dipole field, shown in Figs. 8 and 9.

B. Reconstruction from Individual Frequency Maps

The remote dipole field reconstructed from Planck individual frequency maps at 100, 143, 217, and 353 GHz and unWISE blue galaxies are shown in Fig. 8. All maps contain localized features with an amplitude orders of magnitude larger than the typical fluctuations away from the galactic plane (note the non-linear color scaling in the figures - small amplitudes are linear while large amplitudes are logarithmic). One such feature is a negative amplitude band encompassing the galactic plane. The other are localized spots with a large positive amplitude, confined near the galactic plane. These features are correlated among the different frequencies - the negative amplitude band has nearly the same width/morphology and the positive amplitude features are located at the same positions. The presence of foreground artifacts concentrated near the galactic plane is not surprising given the strong galactic emission in the Planck maps as well as

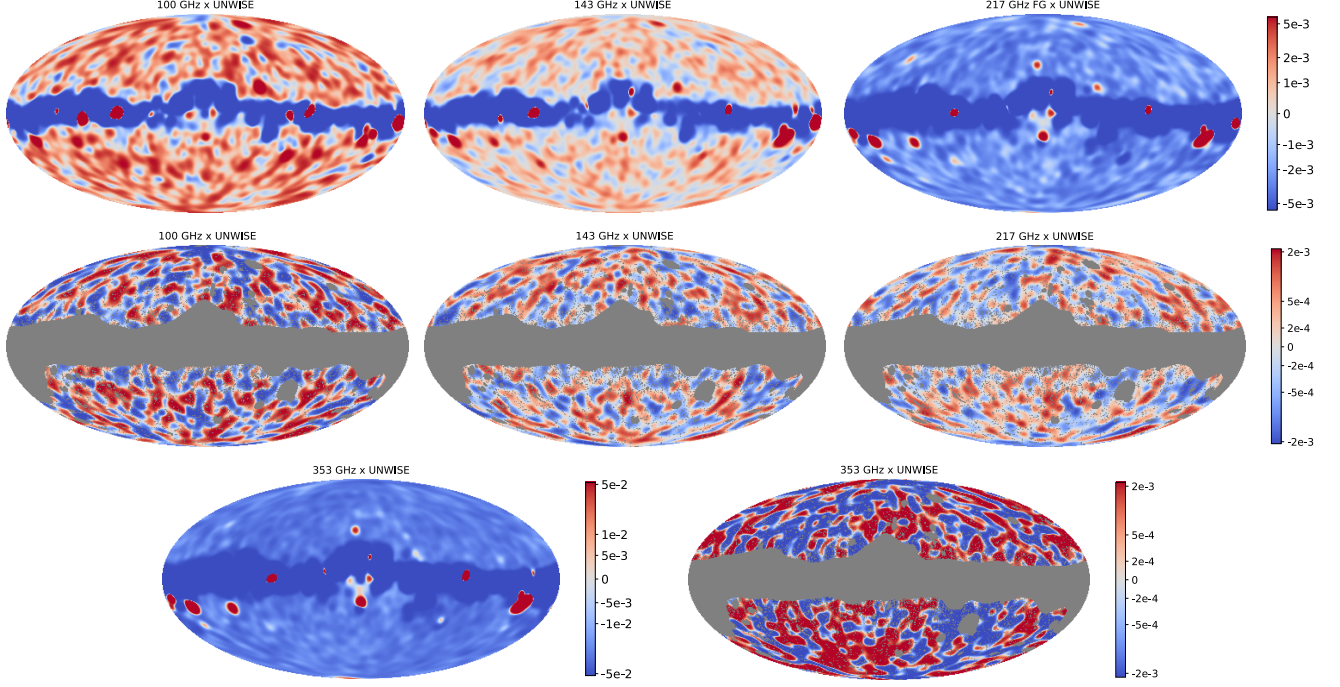


FIG. 8. Dipole field reconstructions based on the Planck 100, 143, 217, and 353 GHz individual frequency maps and the unWISE blue sample in units of v/c and smoothed with a 10° Gaussian beam. Unmasked maps (top row and bottom left) are plotted on a linear scale at low amplitudes and a logarithmic scale at high amplitude. Masked maps (middle row and bottom right) are plotted on a linear scale. Large-amplitude features in the reconstruction confined to the galactic plane are effectively removed by masking. A large monopole (positive for low frequency, negative for high frequency) is visible in the unmasked maps. Masked maps are shown with the dipole and monopole removed. The amplitude of fluctuations is visibly lowest for the masked 217 GHz reconstruction - this is the cleanest channel for kSZ velocity reconstruction.

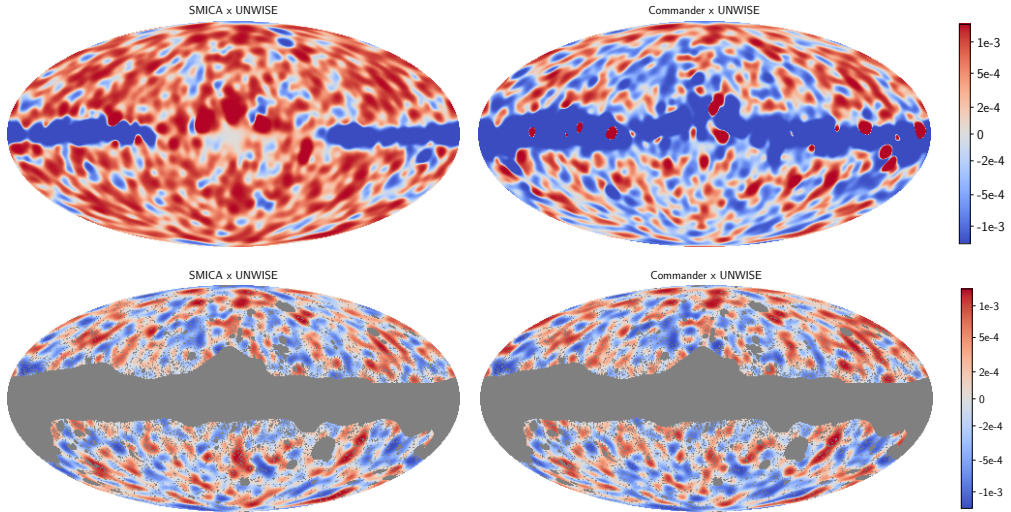


FIG. 9. Dipole field reconstructions based on the Planck SMICA and Commander CMB maps and the unWISE blue sample in units of v/c and smoothed with a 10° Gaussian beam. Unmasked (top row) and masked maps (bottom row) are plotted on a linear scale. As for the individual frequency maps in Fig. 8, large-amplitude features in the reconstruction are effectively removed by masking. A small, positive monopole is visible in the unmasked maps; masked maps are shown with the dipole and monopole removed. Comparing the reconstructions, they are visually highly correlated.

the visible galactic contamination in the unWISE galaxy density (see Fig. 1). The large amplitude features at any frequency are within the reconstruction mask, as seen in Fig. 8 (middle row and bottom-right). The quadratic estimator is highly local (it relies on the small angular-scale cross-correlations), so there is little leakage between contaminated and uncontaminated regions; we conclude that galactic foregrounds can be effectively mitigated by masking.

For further analysis, we apply the reconstruction mask described in Sec. III C. Clearly visible in the individual unmasked frequency maps is a large monopole, which is positive at 100 GHz, almost null at 143 GHz, and increasingly negative at 217 and 353 GHz. As our first step, we therefore use the healpix function `fit_dipole` to estimate and remove the best-fit monopole and dipole from the masked maps. The magnitude of the monopole as well as the magnitude and direction of the dipole are recorded in Table II.

After subtracting the monopole and dipole, we compute the angular power spectra of the masked maps and divide by the f_{sky} of the reconstruction mask to estimate the full-sky power spectrum. As discussed in Sec. III H, for a realization from a purely flat power spectrum, dividing by f_{sky} is the appropriate factor to translate between the cut-sky pseudo- C_ℓ spectrum to the angular power spectrum on the full-sky. The results at each frequency are shown in Fig. 10. Comparing the reconstruction power spectrum (blue) to the expected reconstruction noise (black dashed) computed from Eq. (19) we find good general agreement. Comparing the level of reconstruction noise against the expected signal amplitude (see Fig. 6), our results are consistent with the expectation that our measurements are in the noise-dominated regime.

To investigate the reconstruction power spectrum in greater detail, in Fig. 11 we show the power spectrum of the reconstruction over the full range of multipoles $2 < \ell < 4000$ for the reconstruction based on the 217 GHz channel. The reconstruction power spectrum is very nearly flat for $\ell < 10^3$, consistent with our expectation of a scale-invariant reconstruction noise. However, there is a notable offset between the predicted estimator variance (black solid) and the level of reconstruction power at low ℓ . An offset of a similar magnitude is found across all frequency and component-separated CMB maps.

To determine the origin of this offset, we perform a simple set of simulations as follows. We create random Gaussian realizations of the 217 GHz temperature map and the unWISE galaxy density map from their observed power spectra, rescaled to the expected full-sky values by f_{sky}^{-1} . We then create an optical depth map by filtering the unWISE galaxy density realization in harmonic space by the factor $\tilde{C}_\ell^{\tau g}/C_\ell^{gg}$ and multiply this by a random Gaussian realization of the remote dipole field at the expected amplitude. This approximates the expected kSZ contribution to the CMB from the component of LSS correlated with unWISE. This mock kSZ map is added to the ran-

dom Gaussian primary CMB map. We pass the mock maps through the quadratic estimator pipeline, both on the full sky and with masks corresponding to the 217 GHz analysis.

First, we confirm that the simulations behave as expected on the full sky, producing the correct estimator mean and variance. We find a similar offset to the 217 GHz estimator variance in our simulations only when the power spectra used to filter the temperature and galaxy density in Eq. (20) are empirically determined from masked input maps rather than full-sky empirical or theory spectra. This implies that our analysis could be improved at the $\mathcal{O}(10\%)$ -level by a more careful treatment of the filtering operation and the spectra therein. We defer this to future work. Here, we apply an empirical correction to the estimator normalization taking $N \rightarrow \alpha N$ such that the measured estimator variance equals $C_\ell^{\hat{v}\hat{v}} = \alpha N$ at high- ℓ . The necessary correction factors are listed in Table III, which is the best-fit normalization over the multipole range $2 \leq \ell \leq 200$ where the estimator variance is scale independent.

C. Foreground characterization

Comparing the reconstructions produced from different frequency maps, we can characterize the ways that foregrounds contribute. The clearest impact of foregrounds is on the reconstruction monopole. As discussed in Sec. II C, statistically *isotropic* cross-correlations between the temperature and galaxy map contribute only to the reconstruction monopole. To estimate the contribution from foregrounds, we perform a reconstruction using CMB-subtracted maps obtained using the Commander component separation technique. To estimate the contribution from CMB detector noise, we perform a reconstruction using noise realizations from the FFP10 simulations. In the left panel of Fig. 12, we compare the monopole for the reconstruction based on the temperature maps (blue), CMB-subtracted maps (red), and noise simulations (black). First, we see that detector noise does not contribute to the monopole. At 217 and 353 GHz we obtain a nearly identical monopole from the temperature and CMB-subtracted maps, implying that the measured monopole can be entirely accounted for by foregrounds at high frequency. At 100 GHz, foregrounds do not entirely account for the observed monopole, though it is unclear how significant this offset is.

Similarly, we assess the impact of foregrounds and detector noise on the dipole and higher multipole moments by comparing reconstructions based on temperature, CMB-subtracted, and noise maps in Fig. 12 (right panel) and Fig. 10 respectively. As discussed in detail in Sec. II C, statistically *anisotropic* cross-correlations between the temperature and galaxy maps are necessary to influence the estimator beyond the monopole. Uncorrelated foregrounds and systematics contribute to the estimator variance only through their impact on the recon-

Temperature Map	Monopole [v/c]	Dipole [v/c]	Dipole Direction (l, b)
100 GHz	1.40×10^{-3}	1.34×10^{-4}	$(231.9^\circ, -71.4^\circ)$
143 GHz	3.84×10^{-4}	7.18×10^{-5}	$(54.5^\circ, 46.5^\circ)$
217 GHz	-2.52×10^{-3}	6.39×10^{-5}	$(304.0^\circ, -21.1^\circ)$
353 GHz	-2.10×10^{-2}	3.03×10^{-4}	$(52.8^\circ, -29.4^\circ)$
SMICA	5.42×10^{-4}	2.88×10^{-5}	$(275.3^\circ, 57.0^\circ)$
Commander	-3.41×10^{-5}	1.63×10^{-4}	$(208.9^\circ, 41.3^\circ)$
SMICA x Commander	2.54×10^{-4}	5.81×10^{-5}	N/A

TABLE II. The best-fit monopole and dipole (found using the healpix function `fit_dipole`) for the masked reconstructed dipole field based on various temperature maps correlated with unWISE galaxies. The monopole is defined as the average of the unmasked pixels. The dipole magnitude is defined as the maximum value of the dipolar contribution to the map D_{\max} ; this is related to the $\ell = 1$ harmonic coefficients by $C_{\ell=1}^{v\hat{v}} = (a_{11}^2 + a_{10}^2 + a_{1-1}^2)/3 = 4\pi D_{\max}^2/3$. The dipole direction is the galactic longitude and latitude of the dipole maximum in degrees. For reference, the primary CMB dipole is at $(264^\circ, 48^\circ)$.

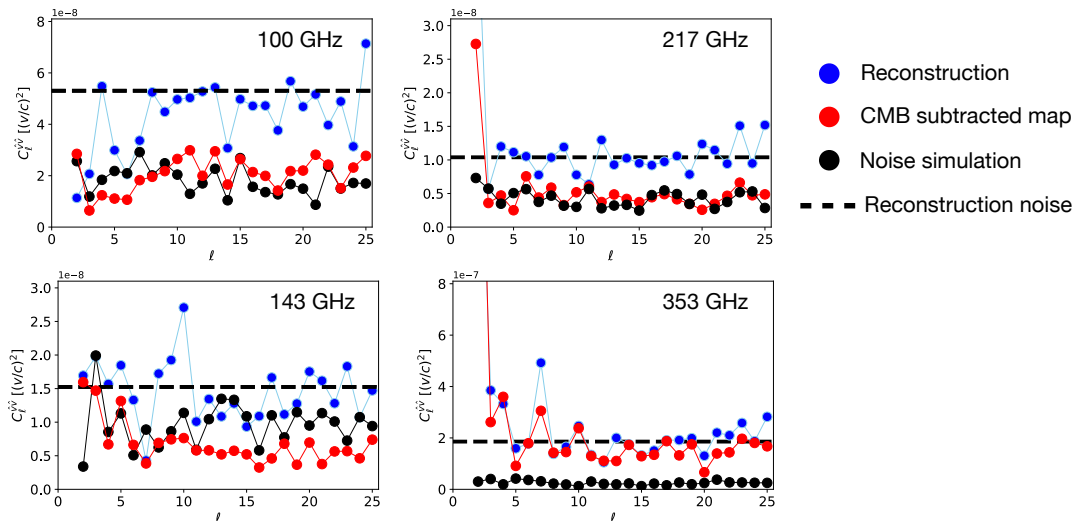


FIG. 10. Power spectra of the masked reconstructed dipole field after the monopole and dipole have been subtracted. The reconstruction power produced using each individual frequency map (blue) is compared to the predicted reconstruction noise N (black dashed) from Eq. (19) that is used to normalize the estimator. To determine how much the primary CMB, foregrounds, and CMB detector noise contribute to the reconstruction variance, we also plot reconstructions using CMB-subtracted maps (red) and a noise realization from the Planck FFP10 simulation suite (black).

Temperature Map	α	$\alpha N [v^2/c^2]$
100 GHz	1.076	5.71×10^{-8}
143 GHz	1.090	1.66×10^{-8}
217 GHz	1.083	1.13×10^{-8}
353 GHz	0.935	1.74×10^{-7}
SMICA	1.118	7.39×10^{-9}
Commander	0.934	6.21×10^{-9}
SMICA x Commander	1.022	6.11×10^{-9}

TABLE III. The correction α to the estimator normalization N necessary for the normalization to equal the estimator variance, and the resulting variance after the correction is applied. The value of α is determined by fitting the reconstruction power spectra to a constant over the range $2 \leq \ell \leq 200$ as described in the text.

struction noise. In the right panel of Fig. 12, we see that reconstructions based on temperature, CMB-subtracted, and noise maps yield a dipole of similar magnitude with

similar frequency dependence. Further, the magnitude and frequency dependence is comparable to what would be expected from the reconstruction noise. Note that cosmic variance at $\ell = 1$ on the reconstruction noise is 80% of the RMS (including the fractional sky coverage). The contribution of foregrounds to the dipole amplitude through N can be estimated by comparing the black and green dashed curves in Fig. 12 - it is only significant at the highest frequencies. Finally, we note that the direction of the best-fit dipole recorded in Table II has a strong frequency dependence. This provides further evidence that foregrounds contribute significantly to the dipole.

Turning to the higher multipoles, the power spectra in Fig. 10 are broadly consistent with reconstruction noise. At 100 and 217 GHz, the reconstruction power spectra based on the CMB subtracted and noise maps yield contributions of a similar magnitude, significantly below the full reconstruction power. We conclude from this that

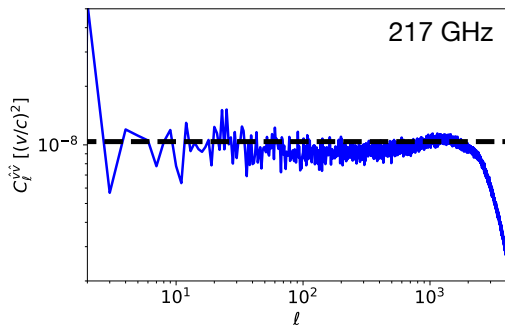


FIG. 11. Power spectrum of the masked, monopole/dipole subtracted, and f_{sky} re-scaled reconstructed dipole field found using the 217 GHz temperature map (blue). The power is nearly flat for $\ell < 10^3$, consistent with the expectation of a constant reconstruction noise. Note however that there is a slight offset in the predicted reconstruction noise (black dashed) and the level of power in the reconstruction. The correction to the estimator normalization that brings these into agreement is recorded in Table III.

the primary CMB is contributing significantly to the estimator variance at these frequencies. At 143 GHz, the power generated by noise is larger than foregrounds, and explains most of the estimator variance. At 353 GHz, foregrounds account for essentially all of the estimator variance - though this is accurately captured by the level of reconstruction noise.

Based on these observations, there is no evidence for an additive bias from foregrounds or systematics of the type introduced in Eqs. (27) and (28) in the data. We conclude that foregrounds can effectively be mitigated by masking, removing the map monopole, and properly accounting for all contributions to temperature maps in the estimator weights and normalization. We stress that this is an extremely optimistic conclusion for the future of kSZ velocity reconstruction/kSZ tomography.

The FFP10 suite of simulations also provide templates for various individual foreground components. By performing the reconstruction on these templates, we can determine the foreground that contributes the most to the estimator response at each frequency. For all FFP10 simulated foreground maps the dominant foreground at 100, 143, 217, and 353 GHz is galactic thermal dust, increasing sharply from small contributions at 100 GHz to large contributions accounting for most of the reconstruction variance at 217 and 353 GHz. At 217 and 353 GHz no other simulated foregrounds are within an order of magnitude of the thermal dust reconstructions at low- ℓ . At 100 and 143 GHz there is some contribution from faint radio point sources, with a larger contribution at 100 GHz where these radio sources are louder than at 143 GHz.

We perform a reconstruction using the 353 GHz CIB maps of Ref. [49] to examine the impact of the CIB on the velocity reconstruction. We apply the union of the unWISE mask and the CIB mask of Ref. [49], which results

in an unmasked sky fraction of $f_{\text{sky}} = 0.18$ concentrated near the galactic poles. Applying this mask also to the FFP10 thermal dust simulation at 353 GHz, we find that the CIB is the dominant foreground by an order of magnitude. For example, the monopole associated with the CIB reconstruction is -3.6×10^{-3} (measured in dimensionless units of v/c) while the monopole associated with the thermal dust reconstruction is -2.5×10^{-4} . This is roughly an order of magnitude smaller than the monopole for thermal dust at 353 GHz using the fiducial mask (see Table II), implying that masking effectively removes the galactic thermal dust contribution to the estimator but the contribution from the CIB remains.

D. Reconstruction from SMICA and Commander CMB maps

The reconstructions using the SMICA and Commander CMB maps are shown in Fig. 9. In contrast to the individual frequency maps, the monopole is rather small for both maps; the best-fit values are recorded in Table II. The SMICA monopole is an order of magnitude larger than the Commander reconstruction monopole (it is visible in the unmasked SMICA map in Fig. 9), but this is still far smaller than the reconstruction monopole found for all frequency maps besides 143 GHz. A relatively small monopole is consistent with the interpretation that SMICA and Commander have smaller statistically isotropic cross-power with unWISE due to foreground removal. In Table II we additionally present the SMICA x Commander (e.g. the average) monopole cross-power.

Turning to the dipole, we find that the SMICA dipole is comparable in magnitude to the expected level of reconstruction noise. The Commander dipole is roughly five times larger. The dot product of the SMICA and Commander dipoles is closer to SMICA (the 'SMICA x Commander' entry in Table II). The direction of both dipoles is similar, and near the direction of the primary CMB dipole at galactic coordinates $(264^\circ, 48^\circ)$. From the present analysis, it is unclear if this is a coincidence or indicates the presence of a systematic or a signal correlated with the CMB dipole.

In Fig. 13 we show the reconstruction spectra for SMICA, Commander, and their cross-power. We include the cross-power to isolate which features in the SMICA and Commander power spectra might arise from systematics associated with the component separation techniques. The spectra have been rescaled by a factor of $\alpha^2 f_{\text{sky}}^{-1}$ to approximate the full-sky power spectrum and ensure the observed estimator variance over the range $2 \leq \ell \leq 200$ is consistent with the estimator pre-factor. The appropriate values of α are recorded in Table III. We have also removed the monopole and dipole described above from the masked map. The spectra are all broadly consistent, sharing distinct features in the power spectra. The consistency is also visible at the map-level - the fea-

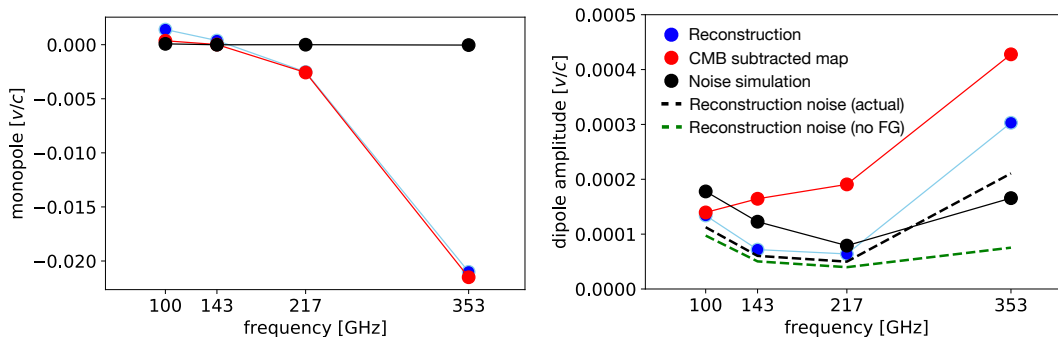


FIG. 12. The monopole (left) and dipole magnitude (right) for masked reconstructions at each frequency (blue) compared with what is obtained from CMB-subtracted maps (red) and simulated CMB detector noise (black). In the right panel, we also plot the expected dipole amplitude from the RMS expected level of reconstruction noise $\sqrt{3N/4\pi}$ for the frequency maps (black dashed) as well as the expected value based on only primary CMB and detector noise (green dashed). The monopole at 217 and 353 GHz is nearly identical for the temperature and CMB-subtracted maps, indicating that foregrounds are dominating the measured monopole at these frequencies. For the dipole, the reconstructions based on temperature, CMB-subtracted, and noise maps contribute at similar levels. Further, the amplitude is consistent with the expected level of reconstruction noise. There is no evidence for additive biases to the estimator.

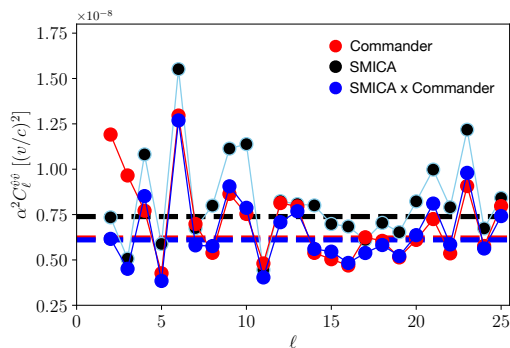


FIG. 13. Power spectra for reconstructions based on SMICA (black), Commander (red), and the cross-power spectrum between SMICA and Commander (blue). The spectra were computed on the masked sky, re-scaled by f_{sky}^{-1} to approximate the power on the full sky, and corrected by the appropriate factor of α^2 from Table III that ensures the estimator variance over the range $2 \leq \ell \leq 200$ is consistent with the estimator pre-factor. We also show the estimator pre-factor αN for SMICA (black dashed), Commander (red dashed) as well as the best-fit cross-power (blue dashed).

tures in the masked reconstructions in Fig. 9 are visibly highly correlated.

The most notable difference between the SMICA and Commander reconstructions is at the very lowest ℓ : Commander has a significantly larger dipole, quadrupole, and octupole than SMICA. Power at these multipoles also lies on the upper range of what might be expected from cosmic variance based on the reconstruction noise. Assessing the significance of this difference is important since a signal at the expected amplitude (see Fig. 6) would produce an excess of power at low- ℓ . If the excess were due to a signal, we might expect that it would appear in the SMICA-Commander cross-spectrum. In Fig. 13, the

cross-spectrum (blue) *does not* include an excess power at low- ℓ . We therefore take the conservative approach of interpreting the low- ℓ excess in Commander as an artifact of the component separation technique. A less conservative possibility is that Commander preserves a real signal, while SMICA removes it. We defer a full exploration of how the various component separation techniques might bias our estimator to future work. Here, we advocate for the most conservative approach: wherever possible, use SMICA x Commander spectra when exploring possible constraints on cosmology from our reconstructions.

We can also examine the one-point statistics of the reconstruction and compare with the theoretical expectation that it should follow the normal product distribution (Eq. (23)). The one-point function for the SMICA and Commander reconstructions is shown in Fig. 14 as compared with the expected normal product distribution using empirical measurements of the pixel variance of the $\xi(\hat{n})$ and $\zeta(\hat{n})$ input filtered fields. Overall, the agreement is quite good, at the $\mathcal{O}(10\%)$ level as shown in the inset. We note that some difference between the empirical one-point function and the normal product distribution is to be expected, since the filtered fields $\xi(\hat{n})$ and $\zeta(\hat{n})$ retain some pixel-pixel correlations and are not themselves Gaussian fields. Coarse-graining to large angular scales, the distribution of pixel values approaches a Gaussian. On the angular scales we consider, it is therefore an excellent approximation to treat the reconstruction as a random Gaussian field that, in the absence of a signal, is fully characterized by the constant estimator variance.

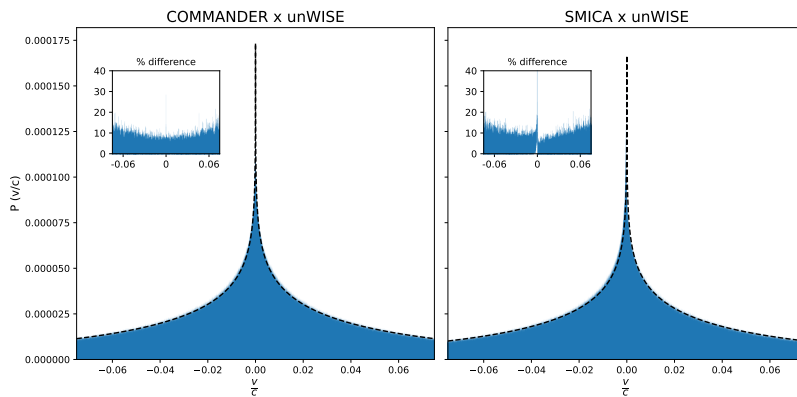


FIG. 14. The one-point function of the dipole field reconstruction plotted against the predicted normal product distribution computed using the filtered map variances (see Eq. (23)). An inset shows the percent difference between the actual and expected one-point distributions; this is smallest near the peak.

E. Cross-correlating the remote dipole reconstruction and unWISE galaxies

As discussed in Sec. III G, the cross-power between the reconstructed remote dipole field and the galaxy density contains additional information about the signal. The cross-power between the SMICA and Commander reconstructions and the unWISE galaxies is shown in Fig. 15. As for the remote dipole autospectra, we have rescaled the remote dipole by the appropriate factor of α , and rescaled the cross-power by a factor of f_{sky}^{-1} to approximate the full-sky cross-power. We also show (dashed lines) the expected variance based on the likelihood for the cross-power (Eq. (15)). For $\ell = 2, 6$ the measured cross-spectra lie outside the plotted range. For $\ell = 2$, the SMICA reconstruction is within the expected variance and positive, while for Commander it is roughly twice the expected power and negative. For $\ell = 6$, both SMICA and Commander are positive and have roughly 3-4 times the expected power.

The measured cross-spectra are generally in agreement with the expected sample variance which is itself large due to large amplitude systematics at low ℓ in the unWISE blue sample. Comparing with Fig. 7, these systematics increase the sample variance on the cross-power by roughly a factor of 5 for $\ell < 10$. Note that our approximation of the full-sky multipoles by multiplying by a simple factor of f_{sky}^{-1} will be sub-optimal on large angular scales. This is in contrast to the reconstruction autospectrum, which does not have significant pixel-pixel correlations. We defer to future work a detailed examination of the cross-spectrum using more sophisticated techniques for power spectrum estimation on the masked sky.

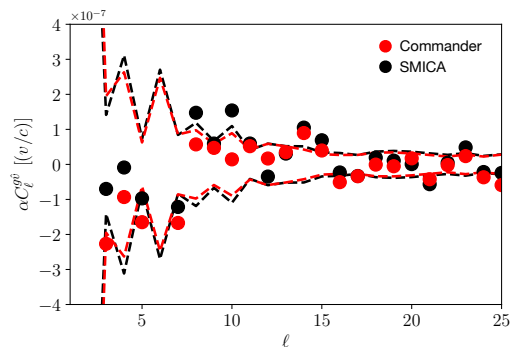


FIG. 15. The cross-power between SMICA (black) and Commander (red) reconstructed dipole fields and the unWISE galaxy density. The cut-sky spectra are scaled by a factor of α and f_{sky}^{-1} to approximate the full-sky cross-power. Data points for $\ell = 2$ and $\ell = 6$ lie outside the plotted range. Also shown are the expected variances (dashed black and red) based on the distribution of Eq. (53) using the empirical unWISE and reconstruction power spectra.

V. CONSTRAINING THE OPTICAL DEPTH BIAS

We now attempt to model and constrain the signal component of the reconstructed remote dipole field. As described in Sec. III H we can find the posterior over b_v (Eq. (56)) by evaluating the product of likelihood functions for the reconstruction power at each multipole over a grid of values for b_v . The result is shown in Fig. 16 for SMICA, Commander, and SMICA x Commander reconstruction spectra, where we have made the following choices in our analysis. We choose $\ell_{\text{min}} = 2$ and $\ell_{\text{max}} = 25$, corresponding to the range of multipoles shown in Fig. 13. We input reconstruction power spectra on the cut-sky rescaled by $\alpha^2 f_{\text{sky}}^{-1}$ to approximate the full-sky spectra. Our theoretical model for the observed spectra (Eq. (55)) uses the computation of the signal C_ℓ^{vv}

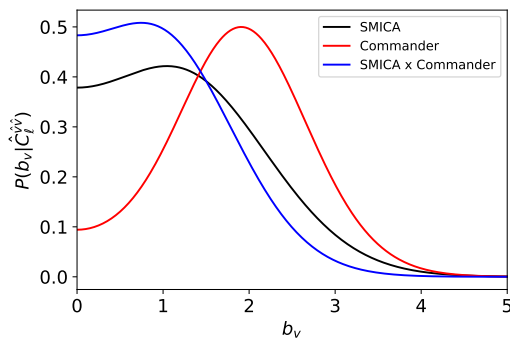


FIG. 16. The posterior probability distribution over b_v from the SMICA (black), Commander (red), and SMICA x Commander (blue) dipole field reconstruction power spectra.

at the fiducial cosmology, unWISE redshift distribution, and galaxy-optical depth cross-power with fixed N set by the α -rescaled estimator prefactor values listed in Table III. We evaluate the posterior in Eq. (56) over a dense grid of values for b_v in the range $0 < b_v < 10$ and compute the normalization by integrating over b_v .

Interpreting the results, we see that the extra power at the first few multipoles in the Commander reconstruction noted in Sec. IV D translates into a peak at non-zero b_v . The posterior for the SMICA and SMICA x Commander reconstructions, with less power at low- ℓ , have a far less-pronounced peak at non-zero b_v . Comparing the ratio of the posterior at its maximum to its value at $b_v = 0$, none of the reconstructions significantly prefers a non-zero value of b_v . This posterior ratio can be equated to the evidence ratio for this simple nested model (e.g. the Savage-Dickey Density Ratio), which yields a result on the Jeffery’s scale corresponding to ‘weak evidence’ for non-zero b_v .

We note that the shape of the distributions are all insensitive to small changes in ℓ_{\max} . Changes in ℓ_{\min} have a larger effect on the distributions. Adding the dipole from Commander has little effect, while adding it for SMICA sharpens the peak around $b_v = 0$ (since the magnitude of the SMICA dipole is relatively small, see Table II). Increasing ℓ_{\min} broadens the distributions as expected, since the signal falls rapidly with ℓ .

We can set an upper limit on b_v by finding the values that encompass 68% and 95% of the posterior; values are recorded in Table IV. As our bottom-line limit on b_v , we choose SMICA x Commander, since this should in principle be the least contaminated by systematic effects. The limit $b_v < 1.40$ at 68% confidence is roughly consistent with our original expectations for an $\mathcal{O}(1)$ total signal-to-noise, as forecasted in Sec III E – the constraint on signal amplitude scales inversely with signal-to-noise. More sensitive data combinations are necessary to establish the detection of a signal.

Temperature Map	68% limit b_v	95% limit b_v
SMICA	1.71	2.90
Commander	2.26	3.22
SMICA x Commander	1.40	2.43

TABLE IV. The correction α to the estimator normalization necessary for the normalization to equal the estimator variance, and the resulting variance after the correction is applied.

VI. CONCLUSIONS

In this paper we have attempted to recover the remote dipole field using kSZ velocity reconstruction applied to CMB temperature data from Planck and galaxy density from the unWISE survey. We adapted the quadratic estimator formalism of Refs. [26–30] to large photometric redshift bins characterizing the unWISE blue sample. We characterized the expected signal, and the impact of possible systematics on the optical depth bias - a multiplicative bias on the estimator mean compared to the expected underlying signal. We applied our reconstruction pipeline to single-frequency Planck temperature maps as well as CMB maps produced from the SMICA and Commander component separation techniques. The reconstructions were used to constrain the amplitude of the velocity bias to $b_v < 1.4$ at 68% confidence, where the fiducial value within Λ CDM with our modelling assumptions is $b_v = 1.0$. This constraint is consistent with our forecasted signal-to-noise of $\mathcal{O}(1)$ for kSZ velocity reconstruction using Planck and the unWISE blue sample.

An important component of our analysis was to characterize the impact of foregrounds and systematics on the reconstruction. A large estimator response is found in the galactic plane across all CMB data products; this can be mitigated by masking. For reconstructions from individual frequency maps, we find a large, frequency-dependent reconstruction monopole in unmasked sky regions. A significant monopole is absent from reconstructions based on component-separated CMB maps. This is consistent with a statistically isotropic cross-correlation between non-blackbody CMB foregrounds and the unWISE galaxy density. Beyond the monopole, there is no statistically significant evidence for additive estimator biases arising from statistically anisotropic cross-correlations between CMB foregrounds and unWISE galaxy density. We therefore conclude that for individual frequency maps, foregrounds can largely be mitigated by masking, accounting for them in the estimator weights and prefactors, and removing the reconstruction monopole.

The masked reconstructions based on different CMB component separation techniques are largely consistent, but with Commander yielding slightly more power than SMICA at multipoles $\ell < 3$. Cross-correlating the reconstructions based on SMICA and Commander yields no excess, indicating that it could be due to low-level systematics associated with the CMB component separation technique. Overall, we conclude that the reconstructions

based on component-separated CMB maps are largely free of systematics and foregrounds, and their spectra – including the monopole and dipole – can be used to constrain the properties of the dipole field.

We quantify the concordance of these reconstructions and a model including a free signal amplitude, the optical depth bias b_v , by computing the posterior shown in Fig. 16. The posteriors based on the individual component separation techniques and their cross-correlation show a mild preference for non-zero b_v , but do not support a claim of detection. We use the posterior based on the cross-correlation between SMICA and Commander reconstructions to derive our bottom-line constraint of $b_v < 1.40$ at 68% confidence.

Even in the absence of a detection, this data is useful for a wide variety of cosmological constraints. The measured reconstruction monopole is sensitive to bulk radial motion, as expected in e.g. void models. The observed reconstruction monopole can thus be seen as a constraint on homogeneity. The reconstruction dipole is the volume-average of the locally observed CMB dipole seen throughout the unWISE survey volume, and is sensitive to large bulk-flows and isocurvature modes. The observed reconstruction dipole can therefore be seen as a measurement of the difference between the rest frame of large-scale structure and the rest frame of the CMB. The cross-correlation between the reconstruction and a galaxy survey can be used to make inferences on large angular scales that are impossibly buried below systematics in the galaxy autopower spectrum. This can place constraints on primordial non-Gaussianity and isocurvature. We explore the constraints on these scenarios in a companion paper [43].

There are several avenues for improving the current analysis. Moving from inverse-variance filtering to Wiener filtering the CMB on the cut sky may address the $\mathcal{O}(10\%)$ offset between the predicted and empirical estimator variance. Another improvement is to utilize better models of the galaxy-optical depth connection (with data-derived constraints on model parameters), and go beyond the linear filtering used to obtain the inferred optical depth map from the galaxy density. We have used only the unWISE blue sample, but applying our pipeline to the green and red samples is straightforward. One could then perform actual ‘tomography’ by using the different redshift distributions to constrain the dipole field at different redshift. Finally, the techniques outlined here can be applied to other existing CMB and galaxy survey datasets. The total signal-to-noise with various data combinations, e.g. ACT and DES, is comparable to the current analysis when trade-offs like sky coverage, CMB detector noise, and galaxy density are taken into account. However, these data combinations allow a more complete exploration of possible systematic effects.

Overall, our results strongly support the future program of kSZ velocity reconstruction/kSZ tomography. We have demonstrated that it is straightforward to mitigate the effects of systematics and foreground in the

quadratic estimator formalism with Planck and unWISE-quality data. Looking ahead to data from Simons Observatory and large photometric surveys such as LSST and SPHEREx, we can expect dramatic improvements. Using spectroscopic surveys such as DESI and in the future MegaMapper, even more dramatic gains in information are possible. In preparation for these new datasets, it will be crucial to refine the analysis pipeline presented here using simulations and also to compare and integrate with complementary techniques and other kSZ estimators (see e.g. the overview in Ref. [28]). We can look forward to a bright future for exploring the most fundamental questions in cosmology using kSZ tomography.

ACKNOWLEDGMENTS

We thank Boris Bolliet, Simone Ferraro, Gil Holder, Selim Hotinli, Fiona McCarthy, Moritz Münchmeyer, Emmanuel Schaan, and Kendrick Smith for helpful input at various stages of this project. In particular we thank Alex Krolewski for providing various unWISE data products and guiding us in their use. MCJ is supported by the National Science and Engineering Research Council through a Discovery grant. Research at Perimeter Institute is supported in part by the Government of Canada through the Department of Innovation, Science and Economic Development Canada and by the Province of Ontario through the Ministry of Research, Innovation and Science. Some of the results in this paper have been derived using the HEALPix package [77].

Appendix A: Estimating the magnitude of the optical depth bias

In this appendix we explore the plausible range over which the optical depth bias is expected to vary. We begin by deriving a formal expression for the optical depth bias. Taking the ensemble-average of the harmonic space quadratic estimator in Eq. (9) we have

$$\langle \hat{v}_{\ell m} \rangle = -N_\ell \sum_{\ell_1 m_1; \ell_2 m_2} (-1)^m \begin{pmatrix} \ell_1 & \ell_2 & \ell \\ m_1 & m_2 & -m \end{pmatrix} G_{\ell_1 \ell_2 \ell} \times \langle \Theta_{\ell_1 m_1} \delta_{\ell_2 m_2} \rangle \quad (\text{A1})$$

Substituting with Eq. (8) and utilizing the properties of the Wigner 3j symbols we have

$$\langle \hat{v}_{\ell m} \rangle^t = \frac{N_\ell}{2\ell + 1} \sum_{\ell_1; \ell_2} G_{\ell_1 \ell_2 \ell} [f_{\ell_1 \ell_2 \ell}]^t \times \int d\chi \frac{[C_{\ell=\bar{\ell}}^{\tau g}(\chi)]^t}{[C_{\ell=\bar{\ell}}^{\tau g}]^t} v_{\ell m}(\chi) \quad (\text{A2})$$

where we have explicitly labeled quantities that depend on the true underlying quantities by the ‘t’ superscript.

Re-arranging this slightly, we have

$$\langle \hat{v}_{\ell m} \rangle^t = \int d\chi b_v(\chi, \ell) W_v(\chi) v_{\ell m}(\chi) \quad (\text{A3})$$

where b_v is the optical depth bias, which in general depends on χ and on scale ℓ , and which is defined as

$$\begin{aligned} b_v(\chi, \ell) &\equiv \frac{\sum_{\ell_1; \ell_2} G_{\ell_1 \ell_2} \int f_{\ell_1 \ell_2} d\ell [\bar{C}_{\ell_2}^{\tau g}]^t / \bar{C}_{\ell_2}^{\tau g}}{\sum_{\ell_1; \ell_2} G_{\ell_1 \ell_2} \int f_{\ell_1 \ell_2} d\ell} \\ &\times \frac{[C_{\ell=\bar{\ell}}^{\tau g}(\chi)]^t \bar{C}_{\ell=\bar{\ell}}^{\tau g}}{C_{\ell=\bar{\ell}}^{\tau g}(\chi) [\bar{C}_{\ell=\bar{\ell}}^{\tau g}]^t} \quad (\text{A4}) \\ &\simeq \frac{\sum_{\ell_1} \frac{2\ell_1+1}{4\pi} \frac{\bar{C}_{\ell_1}^{\tau g} [\bar{C}_{\ell_1}^{\tau g}]^t}{C_{\ell_1}^{TT} C_{\ell_1}^{gg}} [C_{\ell=\bar{\ell}}^{\tau g}(\chi)]^t \bar{C}_{\ell=\bar{\ell}}^{\tau g}}{\sum_{\ell_2} \frac{2\ell_2+1}{4\pi} \frac{(\bar{C}_{\ell_2}^{\tau g})^2}{C_{\ell_2}^{TT} C_{\ell_2}^{gg}} C_{\ell=\bar{\ell}}^{\tau g}(\chi) [\bar{C}_{\ell=\bar{\ell}}^{\tau g}]^t} \end{aligned}$$

The approximation in the last line is valid in the limit where $\ell \ll \ell_1, \ell_2$, which removes the scale-dependence of b_v .

If the true cross-spectra are well-described by our model with different parameter choices, we can use Eq. A4 to estimate the range of values we might plausibly expect the optical depth to take. Specializing to spectra described by Eq. (37), we can write Eq. A4 as

$$\begin{aligned} b_v(\chi) &\simeq \frac{[\bar{n}_{e,0}]^t}{\bar{n}_{e,0}} \frac{b_e(\bar{\chi}, \bar{\ell})}{[b_e(\bar{\chi}, \bar{\ell})]^t} \frac{\sum_{\ell_1} \frac{2\ell_1+1}{4\pi} \frac{(\bar{C}_{\ell_2}^{\tau g})^2}{C_{\ell_1}^{TT} C_{\ell_1}^{gg}} \frac{[b_e(\bar{\chi}, \ell_1)]^t}{b_e(\bar{\chi}, \ell_1)}}{\sum_{\ell_2} \frac{2\ell_2+1}{4\pi} \frac{(\bar{C}_{\ell_2}^{\tau g})^2}{C_{\ell_2}^{TT} C_{\ell_2}^{gg}}} \\ &\times \frac{[b_e(\chi, \bar{\ell})]^t [W_g(\chi)]^t}{b_e(\chi, \bar{\ell}) W_g(\chi)} \quad (\text{A5}) \end{aligned}$$

The factors on the first row are constant, while the factors on the second row depend on χ . For the model variations considered below, it is a reasonable approximation to replace $b_v(\chi)$ by a weighted average over the fiducial $W_v(\chi)$ and neglect the χ -dependence. We define

$$b_v \equiv \int d\chi W_v(\chi) b_v(\chi) \quad (\text{A6})$$

It is straightforward to determine the impact of the various factors contributing to b_v , and to assess their expected relative importance.

- $\frac{[\bar{n}_{e,0}]^t}{\bar{n}_{e,0}}$: The mean electron density today is defined in Eq. (39). Since the baryon abundance is well-measured, the most uncertain parameters in this expression are the gas fraction f_{gas} and the fraction of electrons that are ionized X . In our fiducial model we chose $f_{\text{gas}} = 0.9$, which is plausible based on observational baryon inventories e.g. [11, 78, 79]. We also chose $X = 1$, corresponding to the scenario

where helium is completely ionized in the present Universe. Allowing for the gas fraction to be as low as $\sim 80\%$ and allowing for the scenario where helium is not completely ionized, this factor alone could produce an optical depth bias as small as 0.8.

- Factors involving b_e : The bias factor b_e defined in Eq. (35) depends on three redshift-dependent functions: b_* , k_* , and γ , which control the overall amplitude, the scale at which feedback processes suppress structure, and how abrupt this suppression occurs, respectively. Among the model parameters, we expect b_v to be most sensitive to k_* and γ since b_* is a multiplicative constant that does not vary strongly over the redshifts spanned by unWISE. To provide a simple estimate of the sensitivity of b_v , we retain the fiducial $b_*(z)$ and multiply the redshift-dependent parameters by a constant f in the range $0.2 \leq f \leq 2$ such that $k_*(z) \rightarrow f k_*(z)$ and $\gamma \rightarrow f \gamma(z)$. The result is shown in Fig. 17. Qualitatively, $b_v > 1$ when there is less suppression of structure in the electron distribution than the fiducial model over the relevant scales/redshifts and $b_v < 1$ when there is more. If we consider these model variations as representative of the expected mis-match between our fiducial model and the ‘truth’, then a plausible range we might expect due to modelling the electron-galaxy connection is $0.6 \lesssim b_v \lesssim 1.1$.
- $\frac{[W_g(\chi)]^t}{W_g(\chi)}$: As discussed in Sec. IIID, there is significant uncertainty in the redshift distribution characterizing the unWISE blue sample. Here, we model $[W_g(\chi)]^t$ by the individual realizations of the galaxy window function plotted in Fig. 3. Keeping the other factors that contribute to $b_v(\chi)$ in Eq. (A5) fixed, note that $b_v(\chi) W_v(\chi)$ is simply given by $W_v(\chi)$ as computed with the realizations of the galaxy window function. Because the realizations vary strongly in redshift, we estimate b_v by comparing $C_{\ell}^{\hat{v}\hat{v}}$ computed from the fiducial window function and $[C_{\ell}^{\hat{v}\hat{v}}]^t$ computed from the individual galaxy window function realizations. These spectra are shown in Fig. 18. At low- ℓ , it can be seen that the shape of the power spectrum is retained, and we can estimate $b_v \simeq ([C_{\ell}^{\hat{v}\hat{v}}]^t / C_{\ell}^{\hat{v}\hat{v}})^{1/2}$. This yields a range $0.9 \lesssim b_v \lesssim 1.1$.

From the investigation above, it appears difficult to increase the optical depth bias beyond $b_v \sim 1.1$. The strongest influence in the context of our model is b_e , which can yield an optical depth bias as small as $b_v \sim 0.5$ when there is significant extra suppression in small-scale electron power. We therefore take our conservative, bottom-line plausible range of optical depth bias to be $0.5 < b_v < 1.1$.

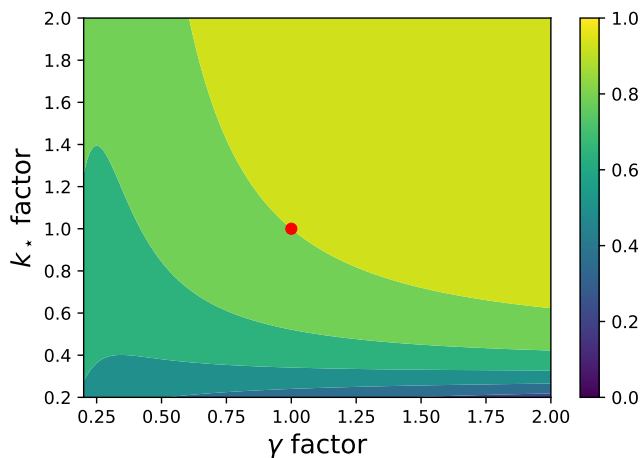


FIG. 17. The weighted average of b_v defined in Eq. (A6) where $[b_e(\chi, \ell)]^t$ is evaluated with $k_*(z)$ and $\gamma(z)$ multiplied by a constant factor (values on the x- and y-axis). The contours shown are for $b_v = \{0.6, 0.7, 0.8, 0.9, 1.0\}$ from dark to light. The red dot indicates the fiducial model.

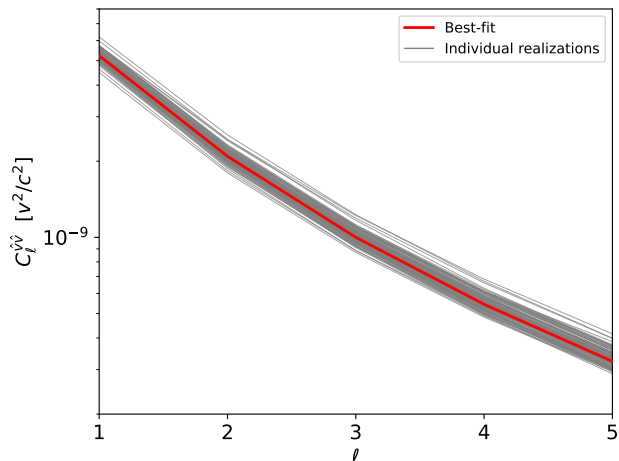


FIG. 18. The estimator autopower spectrum evaluated with individual realizations of the galaxy window function (grey) plotted against the fiducial spectrum (red). The optical depth bias can be estimated as the square root of the ratio of the grey and red curves.

-
- [1] Planck Collaboration, Planck 2018 results. I. Overview and the cosmological legacy of Planck, *Astronomy & Astrophysics* **641**, A1 (2020).
- [2] T. Louis *et al.*, The atacama cosmology telescope: two-season actpol spectra and parameters, *Journal of Cosmology and Astroparticle Physics* **2017** (06), 031–031.
- [3] J. E. Carlstrom *et al.*, The 10 meter south pole telescope, *Publications of the Astronomical Society of the Pacific* **123**, 568 (2011).
- [4] The Simons Observatory Collaboration, The Simons Observatory: science goals and forecasts, *Journal of*

- Cosmology and Astroparticle Physics* **2019** (02), 056, arXiv:1808.07445v2.
- [5] K. N. Abazajian *et al.* (CMB-S4), CMB-S4 Science Book, First Edition, (2016), arXiv:1610.02743 [astro-ph.CO].
- [6] R. A. Sunyaev and Y. B. Zeldovich, The velocity of clusters of galaxies relative to the microwave background. The possibility of its measurement, *Monthly Notices of the Royal Astronomical Society* **190**, 413 (1980).
- [7] N. Hand *et al.*, Evidence of Galaxy Cluster Motions with the Kinematic Sunyaev-Zel’dovich Effect, *Physical Review Letters* **109**, 041101 (2012).

- [8] F. D. Bernardis *et al.*, Detection of the pairwise kinematic Sunyaev-Zel'dovich effect with BOSS DR11 and the Atacama Cosmology Telescope, *Journal of Cosmology and Astroparticle Physics* **2017** (03), 008.
- [9] Z. Chen, P. Zhang, X. Yang, and Y. Zheng, Detection of pairwise kSZ effect with DESI galaxy clusters and Planck, *Monthly Notices of the Royal Astronomical Society* **510**, 5916 (2022), arXiv:2109.04092.
- [10] A. Kusiak, B. Bolliet, S. Ferraro, J. C. Hill, and A. Krolewski, Constraining the baryon abundance with the kinematic Sunyaev-Zel'dovich effect: Projected-field detection using Planck, WMAP, and unWISE, *Phys. Rev. D* **104**, 043518 (2021), arXiv:2102.01068 [astro-ph.CO].
- [11] E. Schaan *et al.* (Atacama Cosmology Telescope Collaboration), Atacama cosmology telescope: Combined kinematic and thermal sunyaev-zel'dovich measurements from boss cmass and lowz halos, *Phys. Rev. D* **103**, 063513 (2021).
- [12] J. C. Hill, S. Ferraro, N. Battaglia, J. Liu, and D. N. Spergel, Kinematic Sunyaev-Zel'dovich Effect with Projected Fields: A Novel Probe of the Baryon Distribution with Planck, WMAP, and WISE Data, *Phys. Rev. Lett.* **117**, 051301 (2016), arXiv:1603.01608 [astro-ph.CO].
- [13] S. Ferraro, J. C. Hill, N. Battaglia, J. Liu, and D. N. Spergel, Kinematic Sunyaev-Zel'dovich effect with projected fields. II. Prospects, challenges, and comparison with simulations, *Phys. Rev. D* **94**, 123526 (2016), arXiv:1605.02722 [astro-ph.CO].
- [14] P. Zhang, The dark flow induced small scale kinetic Sunyaev Zel'dovich effect, *Mon. Not. Roy. Astron. Soc.* **407**, L36 (2010), arXiv:1004.0990 [astro-ph.CO].
- [15] P. Zhang and A. Stebbins, Confirmation of the Copernican Principle at Gpc Radial Scale and above from the Kinetic Sunyaev Zel'dovich Effect Power Spectrum, *Phys. Rev. Lett.* **107**, 041301 (2011), arXiv:1009.3967 [astro-ph.CO].
- [16] P. Zhang and M. C. Johnson, Testing eternal inflation with the kinetic Sunyaev Zel'dovich effect, *JCAP* **06**, 046, arXiv:1501.00511 [astro-ph.CO].
- [17] J. I. Cayuso and M. C. Johnson, Towards testing CMB anomalies using the kinetic and polarized Sunyaev-Zel'dovich effects, *Phys. Rev. D* **101**, 123508 (2020), arXiv:1904.10981 [astro-ph.CO].
- [18] M. Münchmeyer, M. S. Madhavacheril, S. Ferraro, M. C. Johnson, and K. M. Smith, Constraining local non-Gaussianities with kinetic Sunyaev-Zel'dovich tomography, *Physical Review D* **100**, 083508 (2019), arXiv:1810.13424.
- [19] D. Contreras, M. C. Johnson, and J. B. Mertens, Towards detection of relativistic effects in galaxy number counts using kSZ Tomography, *JCAP* **10**, 024, arXiv:1904.10033 [astro-ph.CO].
- [20] N. Anil Kumar, G. Sato-Polito, M. Kamionkowski, and S. C. Hotinli, Primordial trispectrum from kinetic Sunyaev-Zel'dovich tomography, *Phys. Rev. D* **106**, 063533 (2022), arXiv:2205.03423 [astro-ph.CO].
- [21] U.-L. Pen and P. Zhang, Observational Consequences of Dark Energy Decay, *Phys. Rev. D* **89**, 063009 (2014), arXiv:1202.0107 [astro-ph.CO].
- [22] Z. Pan and M. C. Johnson, Forecasted constraints on modified gravity from Sunyaev-Zel'dovich tomography, *Physical Review D* **100**, 083522 (2019), arXiv:1906.04208.
- [23] S. C. Hotinli, J. B. Mertens, M. C. Johnson, and M. Kamionkowski, Probing correlated compensated isocurvature perturbations using scale-dependent galaxy bias, *Physical Review D* **100**, 103528 (2019), arXiv:1908.08953.
- [24] N. A. Kumar, S. C. Hotinli, and M. Kamionkowski, Uncorrelated compensated isocurvature perturbations from kinetic Sunyaev-Zeldovich tomography, *Phys. Rev. D* **107**, 043504 (2023), arXiv:2208.02829 [astro-ph.CO].
- [25] J. Shao, P. Zhang, W. Lin, Y. Jing, and J. Pan, The kinetic SZ tomography with spectroscopic redshift surveys, *Mon. Not. Roy. Astron. Soc.* **413**, 628 (2011), arXiv:1004.1301 [astro-ph.CO].
- [26] A. Terrana, M.-J. Harris, and M. C. Johnson, Analyzing the cosmic variance limit of remote dipole measurements of the cosmic microwave background using the large-scale kinetic Sunyaev Zel'dovich effect, *Journal of Cosmology and Astroparticle Physics* **2017** (02), 040, arXiv:1610.06919v2.
- [27] A.-S. Deutsch, E. Dimastrogiovanni, M. C. Johnson, M. Münchmeyer, and A. Terrana, Reconstruction of the remote dipole and quadrupole fields from the kinetic Sunyaev Zel'dovich and polarized Sunyaev Zel'dovich effects, *Physical Review D* **98**, 123501 (2018).
- [28] K. M. Smith, M. S. Madhavacheril, M. Münchmeyer, S. Ferraro, U. Giri, and M. C. Johnson, KSZ tomography and the bispectrum, (2018), arXiv:1810.13423.
- [29] J. I. Cayuso, M. C. Johnson, and J. B. Mertens, Simulated reconstruction of the remote dipole field using the kinetic Sunyaev Zel'dovich effect, *Physical Review D* **98**, 063502 (2018), arXiv:1806.01290.
- [30] J. Cayuso, R. Bloch, S. C. Hotinli, M. C. Johnson, and F. McCarthy, Velocity reconstruction with the cosmic microwave background and galaxy surveys, *Journal of Cosmology and Astroparticle Physics* **2023** (02), 051, arXiv:2111.11526.
- [31] Y. Kvasiuk and M. Münchmeyer, Autodifferentiable likelihood pipeline for the cross-correlation of CMB and large-scale structure due to the kinetic Sunyaev-Zeldovich effect, *Phys. Rev. D* **109**, 083515 (2024), arXiv:2305.08903 [astro-ph.CO].
- [32] D. Contreras, F. McCarthy, and M. C. Johnson, Maximum likelihood kinetic Sunyaev-Zel'dovich velocity reconstruction, *Phys. Rev. D* **107**, 023521 (2023), arXiv:2205.15779 [astro-ph.CO].
- [33] U. Giri and K. M. Smith, Exploring KSZ velocity reconstruction with N-body simulations and the halo model, *JCAP* **09**, 028, arXiv:2010.07193 [astro-ph.CO].
- [34] LSST Science and LSST Project Collaborations, LSST Science Book, Version 2.0, (2009), arXiv:0912.0201.
- [35] A. Aghamousa *et al.* (DESI), The DESI Experiment Part I: Science, Targeting, and Survey Design, (2016), arXiv:1611.00036 [astro-ph.IM].
- [36] E. L. Wright *et al.*, The Wide-field Infrared Survey Explorer (WISE): Mission Description and Initial On-orbit Performance, *The Astronomical Journal* **140**, 1868 (2010), arXiv:1008.0031 [astro-ph.IM].
- [37] A. Mainzer *et al.*, Initial Performance of the NEOWISE Reactivation Mission, *The Astrophysical Journal* **792**, 30 (2014), arXiv:1406.6025.
- [38] D. Lang, unwise: Unblurred coadds of the wise imaging, *The Astronomical Journal* **147**, 108 (2014).
- [39] A. M. Meisner, D. Lang, and D. J. Schlegel, Full-depth coadds of the wise and first-year neowise-reactivation im-

- ages, *The Astronomical Journal* **153**, 38 (2017).
- [40] A. M. Meisner, D. Lang, and D. J. Schlegel, Deep full-sky coadds from three years of wise and neowise observations, *The Astronomical Journal* **154**, 161 (2017).
- [41] E. F. Schlafly, A. M. Meisner, and G. M. Green, The unwise catalog: Two billion infrared sources from five years of wise imaging, *The Astrophysical Journal Supplement Series* **240**, 30 (2019).
- [42] A. Krolewski, S. Ferraro, E. F. Schlafly, and M. White, unWISE tomography of Planck CMB lensing, *Journal of Cosmology and Astroparticle Physics* **2020** (05), 047, arXiv:1909.07412v2.
- [43] R. Bloch, S. C. Hotinli, J. Krywonos, and M. C. Johnson, Cosmological constraints from ksz tomography, to appear.
- [44] N. Battaglia, The Tau of Galaxy Clusters, *JCAP* **08**, 058, arXiv:1607.02442 [astro-ph.CO].
- [45] Y. Akrami *et al.* (Planck), Planck intermediate results. LVI. Detection of the CMB dipole through modulation of the thermal Sunyaev-Zeldovich effect: Eppur si muove II, *Astron. Astrophys.* **644**, A100 (2020), arXiv:2003.12646 [astro-ph.CO].
- [46] Y. Akrami *et al.* (Planck), Planck 2018 results. IV. Diffuse component separation, *Astron. Astrophys.* **641**, A4 (2020), arXiv:1807.06208 [astro-ph.CO].
- [47] H. K. Eriksen, J. B. Jewell, C. Dickinson, A. J. Banday, K. M. Górski, and C. R. Lawrence, Joint bayesian component separation and cmb power spectrum estimation, *The Astrophysical Journal* **676**, 10 (2008).
- [48] P. A. R. Ade *et al.* (Planck), Planck 2015 results. XII. Full Focal Plane simulations, *Astron. Astrophys.* **594**, A12 (2016), arXiv:1509.06348 [astro-ph.CO].
- [49] D. Lenz, O. Doré, and G. Lagache, Large-scale Maps of the Cosmic Infrared Background from Planck, *The Astrophysical Journal* **883**, 75 (2019), arXiv:1905.00426.
- [50] M. Tegmark, A. De Oliveira-Costa, and A. J. Hamilton, High resolution foreground cleaned CMB map from WMAP, *Physical Review D* **68**, 123523 (2003).
- [51] S. Ferraro, B. D. Sherwin, and D. N. Spergel, WISE measurement of the integrated Sachs-Wolfe effect, *Phys. Rev. D* **91**, 083533 (2015), arXiv:1401.1193 [astro-ph.CO].
- [52] G. A. Marques and A. Bernui, Tomographic analyses of the CMB lensing and galaxy clustering to probe the linear structure growth, *JCAP* **05**, 052, arXiv:1908.04854 [astro-ph.CO].
- [53] A. Krolewski, S. Ferraro, and M. White, Cosmological constraints from unwise and planck cmb lensing tomography, *Journal of Cosmology and Astroparticle Physics* **2021** (12), 028.
- [54] A. Krolewski and S. Ferraro, The Integrated Sachs Wolfe effect: unWISE and Planck constraints on dynamical dark energy, *JCAP* **04** (04), 033, arXiv:2110.13959 [astro-ph.CO].
- [55] A. Kusiak, B. Bolliet, A. Krolewski, and J. C. Hill, Constraining the galaxy-halo connection of infrared-selected unWISE galaxies with galaxy clustering and galaxy-CMB lensing power spectra, *Phys. Rev. D* **106**, 123517 (2022), arXiv:2203.12583 [astro-ph.CO].
- [56] G. S. Farren, B. D. Sherwin, B. Bolliet, T. Namikawa, S. Ferraro, and A. Krolewski, Detection of the CMB lensing – galaxy bispectrum, (2023), arXiv:2311.04213 [astro-ph.CO].
- [57] G. S. Farren *et al.* (ACT), The Atacama Cosmology Telescope: Cosmology from cross-correlations of unWISE galaxies and ACT DR6 CMB lensing, (2023), arXiv:2309.05659 [astro-ph.CO].
- [58] Z. Yan, A. S. Maniyar, and L. van Waerbeke, The star formation, dust, and abundance of galaxies with unWISE-CIB cross-correlations, (2023), arXiv:2310.10848 [astro-ph.CO].
- [59] Gaia Collaboration, Gaia Data Release 2, *Astronomy & Astrophysics* **616**, A1 (2018), arXiv:1804.09365.
- [60] Planck Collaboration, Planck 2018 results. IV. Diffuse component separation, *Astronomy & Astrophysics* **641**, A4 (2020).
- [61] M. S. Madhavacheril, N. Battaglia, K. M. Smith, and J. L. Sievers, Cosmology with the kinematic Sunyaev-Zeldovich effect: Breaking the optical depth degeneracy with fast radio bursts, *Phys. Rev. D* **100**, 103532 (2019), arXiv:1901.02418 [astro-ph.CO].
- [62] C. Laigle *et al.*, The COSMOS2015 Catalog: Exploring the $1 < z < 6$ Universe with half a million galaxies, *Astron. Astrophys. J. Suppl.* **224**, 24 (2016), arXiv:1604.02350 [astro-ph.GA].
- [63] R. Takahashi, K. Ioka, A. Mori, and K. Funahashi, Statistical modelling of the cosmological dispersion measure, *Monthly Notices of the Royal Astronomical Society* **502**, 2615 (2020), arXiv:2010.01560.
- [64] F. Calura, E. Tescari, V. D’Odorico, M. Viel, S. Cristiani, T.-S. Kim, and J. S. Bolton, The Lyman α forest flux probability distribution at $z > 3$, *Monthly Notices of the Royal Astronomical Society* **422**, 3019 (2012).
- [65] M. Viel, G. D. Becker, J. S. Bolton, and M. G. Haehnelt, Warm dark matter as a solution to the small scale crisis: New constraints from high redshift Lyman-alpha forest data, *Physical Review D* **88**, 10.1103/physrevd.88.043502 (2013).
- [66] E. Boera, M. T. Murphy, G. D. Becker, and J. S. Bolton, Constraining the temperature–density relation of the intergalactic medium with the Lyman α and β forests, *Monthly Notices of the Royal Astronomical Society: Letters* **456**, L79 (2015).
- [67] P. R. Upton Sanderbeck, A. D’Aloisio, and M. J. McQuinn, Models of the thermal evolution of the intergalactic medium after reionization, *Monthly Notices of the Royal Astronomical Society* **460**, 1885 (2016).
- [68] P. La Plante, H. Trac, R. Croft, and R. Cen, Helium reionization simulations. ii. signatures of quasar activity on the IGM, *The Astrophysical Journal* **841**, 87 (2017).
- [69] P. La Plante, H. Trac, R. Croft, and R. Cen, Helium reionization simulations. iii. the Helium Ly α forest, *The Astrophysical Journal* **868**, 106 (2018).
- [70] J. S. Bolton, E. Puchwein, D. Sijacki, M. G. Haehnelt, T.-S. Kim, A. Meiksin, J. A. Regan, and M. Viel, The Sherwood simulation suite: overview and data comparisons with the Lyman alpha forest at redshifts $2 \leq z \leq 5$, *Monthly Notices of the Royal Astronomical Society* **464**, 897 (2016).
- [71] S. C. Hotinli, S. Ferraro, G. P. Holder, M. C. Johnson, M. Kamionkowski, and P. La Plante, Probing Helium reionization with kinetic Sunyaev-Zel’dovich tomography, *Phys. Rev. D* **107**, 103517 (2023), arXiv:2207.07660 [astro-ph.CO].
- [72] S. C. Hotinli, Cosmological probes of Helium reionization, *Phys. Rev. D* **108**, 043528 (2023), arXiv:2212.08004 [astro-ph.CO].
- [73] M. Çalışkan, N. Anil Kumar, S. C. Hotinli, and M. Kamionkowski, Reconstructing patchy Helium reion-

- ization using the cosmic microwave background and large-scale structure, (2023), arXiv:2312.00118 [astro-ph.CO].
- [74] A. L. Erickcek, S. M. Carroll, and M. Kamionkowski, Superhorizon Perturbations and the Cosmic Microwave Background, *Phys. Rev. D* **78**, 083012 (2008), arXiv:0808.1570 [astro-ph].
- [75] E. Alizadeh and C. M. Hirata, How to detect gravitational waves through the cross correlation of the galaxy distribution with the cmb polarization, *Physical Review D* **85** (2012).
- [76] C. L. Reichardt *et al.*, A Measurement of Secondary Cosmic Microwave Background Anisotropies with Two Years of South Pole Telescope Observations, *Astrophys. J.* **755**, 70 (2012), arXiv:1111.0932 [astro-ph.CO].
- [77] K. M. Górski, E. Hivon, A. J. Banday, B. D. Wandelt, F. K. Hansen, M. Reinecke, and M. Bartelmann, HEALPix: A Framework for High-Resolution Discretization and Fast Analysis of Data Distributed on the Sphere, *Astrophys. J.* **622**, 759 (2005), arXiv:astro-ph/0409513 [astro-ph].
- [78] M. Fukugita and P. J. E. Peebles, The Cosmic Energy Inventory, *Astrophys. J.* **616**, 643 (2004), arXiv:astro-ph/0406095 [astro-ph].
- [79] J. M. Shull, B. D. Smith, and C. W. Danforth, The Baryon Census in a Multiphase Intergalactic Medium: 30% of the Baryons May Still be Missing, *Astrophys. J.* **759**, 23 (2012), arXiv:1112.2706 [astro-ph.CO].